The Arctic Ocean in summer: A quasi-synoptic inverse estimate of boundary fluxes and water mass transformation

T. Tsubouchi,[1] S. Bacon,[1] A. C. Naveira Garabato,[2] Y. Aksenov,[1] S. W. Laxon,[3] E. Fahrbach,[4] A. Beszczynska-Möller,[4] E. Hansen,[5] C. M. Lee,[6] and R. B. Ingvaldsen[7]

Received 1 April 2011; revised 31 October 2011; accepted 21 November 2011; published 31 January 2012.

[1] The first quasi-synoptic estimates of Arctic Ocean and sea ice net fluxes of volume, heat and freshwater are calculated by application of an inverse model to data around the ocean boundary. Hydrographic measurements from four gateways to the Arctic (Bering, Davis, and Fram Straits and the Barents Sea Opening) completely enclose the ocean, and were made within the same 32-day period in summer 2005. The inverse model is formulated as a set of full-depth and density-layer-specific volume and salinity transport conservation equations, with conservation constraints also applied to temperature, but only in non-outcropping layers. The model includes representations of Fram Strait sea ice export and of interior Arctic Ocean diapycnal fluxes. The results show that in summer 2005 the transport-weighted mean properties are, for water entering the Arctic: potential temperature 4.49°C, salinity 34.50 and potential density (σ_0) 27.34 kg m^{-3}; and for water leaving the Arctic, including sea ice: 0.25°C, 33.81, and 27.13 kg m^{-3}, respectively. The net effect of the Arctic in summer is to freshen and cool the inflows by 0.69 in salinity and 4.23°C, respectively, and to decrease density by 0.21 kg m^{-3}. The volume transport into the Arctic of waters above ~1000 m depth is 9.2 Sv (1 Sv = 10^6 m^3 s^{-1}), and the export (similarly) is 9.3 Sv. The net oceanic and sea ice freshwater flux is 187 ± 48 mSv. The net heat flux (including sea ice) is 189 ± 37 TW, representing loss from the ocean to the atmosphere.

Citation: Tsubouchi, T., S. Bacon, A. C. Naveira Garabato, Y. Aksenov, S. W. Laxon, E. Fahrbach, A. Beszczynska-Möller, E. Hansen, C. M. Lee, and R. B. Ingvaldsen (2012), The Arctic Ocean in summer: A quasi-synoptic inverse estimate of boundary fluxes and water mass transformation, *J. Geophys. Res.*, *117*, C01024, doi:10.1029/2011JC007174.

1. Introduction

[2] The Arctic is an important part of the global climate system through surface reflectivity, storage and release of freshwater (FW), and storage and release of greenhouse gases. However, climate models confidently predict not only that it will change rapidly as the planet warms, but also that it will be the fastest-warming region of the planet [*Intergovernmental Panel on Climate Change*, 2007]. The well-known ice-albedo feedback mechanism results in "polar amplification," and the signal of polar amplification in the Arctic is beginning to emerge from the noise [*Serreze et al.*, 2009].

[3] Many indicators show the response of Arctic climate to warming. For example, September sea ice extent continues to decline at over 1% per year (J. Richter-Menge and J. E. Overland (Eds.), Arctic report card 2011, http://www.arctic.noaa.gov/reportcard, 2011); the Greenland ice cap melt rate is increasing [*Velicogna*, 2009; *van den Broeke et al.*, 2009]; Russian river discharge into the Arctic Ocean continues to increase [*Shiklomanov and Lammers*, 2009]; FW storage in the Arctic Ocean's upper layers has increased [*McPhee et al.*, 2009; *Rabe et al.*, 2011]; *Serreze et al.* [2009] find significant surface warming in Autumn in recent years.

[4] Therefore the importance of ocean and sea ice FW and heat fluxes to the climate system is clear. However, neither of these quantities is well known. Many authors (we will not review them here) make measurements of components of the system and attempt to draw conclusions about heat and FW fluxes from their component observations, but they are hampered in their efforts to integrate their conclusions in a pan-Arctic sense through three issues: (1) reference values (reference temperature for heat flux, reference salinity for FW flux), (2) synopticity (when attempting to compare with other measurements), and (3) pan-Arctic mass balance,

[1]National Oceanography Centre, Southampton, Southampton, UK.
[2]National Oceanography Centre, Southampton, University of Southampton, Southampton, UK.
[3]Centre for Polar Observation and Modelling, University College London, London, UK.
[4]Alfred Wegener Institute for Polar and Marine Research, Bremerhaven, Germany.
[5]Norwegian Polar Institute, Tromsø, Norway.
[6]Polar Science Center, Applied Physics Laboratory, University of Washington, Seattle, Washington, USA.
[7]Institute of Marine Research, Bergen, Norway.

0148-0227/12/2011JC007174

without which net flux calculations are meaningless. While recognizing these difficulties, substantial efforts have been made to calculate Arctic heat and FW budgets.

[5] An Arctic FW budget was first produced by *Aagaard and Carmack* [1989], subsequently updated by *Serreze et al.* [2006] and *Dickson et al.* [2007]. *Serreze et al.* [2006] found net Arctic Ocean FW export of 9,200 km^3 yr^{-1} and import of 8,500 km^3 yr^{-1}, and a net imbalance of -700 km^3 yr^{-1} (292 mSv, 270 mSv and 22 mSv respectively), using a reference salinity of 34.8, and using a large inventory of component data from a wide range of periods. Via an analogous process of accounting, and with alternative views on a suitable reference salinity, the Arctic FW export estimate of *Dickson et al.* [2007] is "around 300 mSv." Note that 1 Sv = 10^6 m^3 s^{-1} = 31,536 km^3 yr^{-1}, so 300 mSv $\sim$ 9,500 km^3 yr^{-1}. While these two modern estimates appear consistent, they cover different areas. *Serreze et al.* [2006] comprises the Arctic Ocean north of Eurasia and North America (therefore north of the Canadian Arctic Archipelago), while *Dickson et al.* [2007] extend some way south on the Atlantic side to include the Nordic Seas and Hudson Bay regions. The sum total FW flux of *Dickson et al.* [2007], considering oceanic and sea ice transports through Bering, Davis and Fram Straits, and the Barents Sea Opening (BSO), is 149–237 mSv (4,725–7,515 km^3 yr^{-1}), where the range results from the given ranges of Davis and Fram Strait fluxes.

[6] The Arctic Ocean and sea ice heat flux was consistently estimated by *Serreze et al.* [2007], furthering the pioneering efforts of *Nakamura and Oort* [1988]. *Serreze et al.* [2007] use atmospheric model reanalysis output with top-of-the-atmosphere (TOA) radiation measurements to produce monthly estimates of ocean surface heat flux as residuals. They find values ranging from 105 W m^{-2} (July, heat gained by ocean from atmosphere) to *ca.* -50 W m^{-2} (winter months, heat lost by ocean to atmosphere), which, for their ocean domain area of 9.56×10^6 km^2, equate to net surface heat fluxes of *ca.* 1,000 TW and -480 TW. Their annual mean (ocean domain) surface heat flux is 11 W m^{-2} from ocean to atmosphere, or 105 TW. They also describe substantial shortcomings with the method, such as nonconservative energy budgets, deficiencies in TOA radiation, and mass balance errors in atmospheric transports.

[7] Turning to the Arctic Ocean mass budget, the most recently produced estimates of annual mean volume flux in the four main ocean gateways are: Davis Strait, -2.3 ± 0.7 Sv during 2004–2005 [*Curry et al.*, 2011]; Fram Strait, -2.0 ± 2.7 Sv mainly during 1997–2006 [*Schauer et al.*, 2008]; BSO, 2.0 Sv mainly during 1997–2007 [*Smedsrud et al.*, 2010]; and Bering Strait, 0.8 ± 0.2 Sv during 1991–2004 [*Woodgate et al.*, 2005; *Melling et al.*, 2008]; sign convention is negative for export (out of Arctic), positive for import. The sum total of all values is -1.5 Sv. Clearly this is not satisfactory for an attempt to make direct estimates of ocean and sea ice heat and FW fluxes as mass is not conserved. However, our motivation for wishing to attempt the estimation of in situ ocean and sea ice heat and FW fluxes is clear from the state of knowledge of these quantities, described above; and the method we choose–inverse modeling–is motivated by this imbalance.

[8] Since 2004, hydrographic observations have been carried out in all four main gateways–Davis, Fram, and Bering Straits, and the BSO–in every summer. Moored arrays of current meters are also deployed in these locations. Therefore we have available temperature and salinity profiles, and a quantity of velocity information. In some regions where some or all of this information is lacking, we can also employ output from a high-resolution coupled ice-ocean general circulation model (GCM). In this study, we will assemble the available quasi-synoptic data and estimate a velocity field in summer 2005 around the boundary of the Arctic Ocean that conserves volume and salinity by applying the box inverse method. The year 2005 is chosen as the first summer when the most comprehensive observations are available around the boundary of the Arctic. We will use the results of the inverse model to present the first quasi-synoptic in situ estimates of Arctic heat and FW fluxes. The model will also enable us to describe Arctic Ocean net water mass transformations.

[9] This paper is structured as follows. Section 2 presents the measurements and the inverse model; section 3 describes the derived velocity field and associated heat and FW fluxes; section 4 is a discussion and summary.

2. Methods

[10] Inverse models are used to determine the ocean circulation that is consistent both with observations and with dynamical and thermodynamical constraints. Inverse modeling began life in the late 1960s as a means to solve geophysical problems. It found its application to oceanography in the late 1970s, since when it has become a common tool routinely applied in oceanography throughout the world's oceans [*Wunsch*, 1996], with one major exception: this is its first quasi-synoptic application to the Arctic Ocean. Accordingly we first outline the inverse model fundamentals.

[11] We use the "box model" formalism, where the box is a region of ocean completely enclosed on its sides by coastline and/or hydrographic sections. The box includes the seabed as its impermeable base and the sea surface as its permeable lid. The sides of our Arctic Ocean box are comprised of the four ocean gateways–Bering, Davis, and Fram Straits, and the BSO, and the intervening coasts of the islands of Greenland and Svalbard, and of the continents of Eurasia and North America. There is one extremely small gap in this continuous boundary, Fury and Hecla Strait, between Baffin Island and the Canadian mainland, which will be described further in section 3.5. The permeable lid accommodates the air-sea heat flux, and the freshwater fluxes resulting from evaporation, precipitation and river/meltwater runoff. The ocean is assumed to be in quasi-steady state, and in hydrostatic and geostrophic balance; it is assumed to be mass- and salinity-conserving. By use of a closed box and the application of mass and salinity conservation constraints, our inverse model generates perturbations–within a priori uncertainties–to the initial horizontal and vertical velocities that are consistent with the conservation conditions.

[12] We first examine the assumptions of mass and salinity conservation over the Arctic Ocean box, and derive the necessary conservation equations in order to clarify the role of "reference values." We also determine the extent to which conservation of heat may be applicable. Next we present the

inverse model, and finally we describe the data and numerical model output employed in the inverse model.

2.1. Conservation Conditions

[13] We first examine mass balance. A mass imbalance in an enclosed region might be generated (for example) by a transient wind event near the region's boundary. In order to estimate the adjustment timescales over which stationarity (in this case, mass balance) may be assumed, we need to calculate relevant barotropic wave propagation speeds. Kelvin and gravity waves are fast, with phase speeds $\sqrt{gH}$, where g is acceleration due to gravity and H is water depth. For g = 10 m s^{-2} and $H \sim$ 1 km, consequent speeds of 100 m s^{-1} result in waves which travel 1,000 km (scale distance for the Arctic) in ~3 h. Barotropic Rossby waves are slower, with an upper bound on phase speed c given by

$$c = \frac{\beta g H}{f_0^2}, \tag{1}$$

where β is the meridional gradient of the Coriolis parameter f such that $\beta = 2\Omega\cos\theta/R_E$, Ω is the rotation rate of the Earth, R_E is the radius of the Earth and θ latitude, and $f_0 = 2\Omega\sin\theta$. For 80°N, $\beta \sim 5 \times 10^{-12}$ m^{-1} s^{-1}, $f_0 \sim 1.5 \times 10^{-4}$ s^{-1}, and as above $gH \sim 10^4$ m^2 s^{-2}, yielding a phase speed $c \sim 2$ m s^{-1}, and a timescale to travel 1,000 km of ~6 days [see, e.g., *Gill*, 1983]. Mass conservation is allowed as long as we do not use an unfeasibly short timescale.

[14] We express the Arctic Ocean mass balance as follows. For an enclosed volume of ocean, the net rate of addition (or removal) of FW at the sea surface by all processes is denoted by F. Assuming conservation of mass (volume), and denoting net ocean flux through the sides of the volume by V_0

$$F + V_0 = 0 \tag{2a}$$

and

$$V_0 = \oint v dA, \tag{2b}$$

where $v = v(x, z)$ is the distribution of ocean velocity normal to the sides of the volume, x is the along-side distance coordinate, z is the vertical (depth) coordinate, area A represents the side area and $dA = dxdz$ is an area element.

[15] We now derive the calculation of surface FW flux F from volume and salinity fluxes, assuming volume and salinity conservations. The net import (or export) of salinity (S) through the ocean boundaries of the enclosed region is equal to the rate of change of salinity storage inside the region, assuming no significant surface or seabed pathways for salinity addition or removal

$$\oint vSdA - \frac{\partial}{\partial t}\oint Sd(vol) = 0, \tag{3}$$

where $d(vol)$ is a volume element. Now we decompose v and S around the boundary into means (overbar) and deviations from means (prime)

$$S = \bar{S} + S' \tag{4a}$$

and

$$v = \bar{v} + v' \tag{4b}$$

such that

$$\oint S' dA = 0 \quad \text{and} \quad \oint v' dA = 0. \tag{5}$$

Using the above to expand (3), we have

$$\frac{\partial}{\partial t}\oint Sd(vol) = \oint (\bar{S} + S')(\bar{v} + v')dA = \bar{S}V_0 + \oint S'v'dA, \tag{6}$$

since the cross-terms (the means multiplied by the integrals of the anomalies) are identically zero. Applying (2) to (6) and rearranging, we have

$$F = \frac{\oint S'v'dA}{\bar{S}} - \frac{\frac{\partial}{\partial t}\oint Sd(vol)}{\bar{S}}. \tag{7}$$

The first term on the right-hand side is similar to the conventional expression for the estimation of FW flux, but the term implicitly performing the role of "reference salinity" is a clearly defined quantity: the boundary-mean salinity. The second term is "storage," the rate of change of internal salinity (scaled by boundary-mean salinity), which we call F_{stor}. For the application of the inverse model, we assume $F_{stor} = 0$. This assumption is examined in section 3.5.

[16] Finally, we consider the possibility of some limited application of heat conservation, given that monthly/annual mean air-sea heat fluxes are not well known. Not wishing to constrain by heat conservation the circulation of any part of the ocean that may be in contact with the atmosphere in any part of the year, we inspect the (near-) surface distribution of density in winter (Figure 1), when surface densities are at a maximum and contact with the atmosphere has (ultimately) its deepest influence on the ocean. Figure 1 shows the winter potential density distribution at 10 m depth based on the Polar Science Centre Hydrographic T/S Climatology (PHC); [*Steele et al.*, 2001]. The densest surface outcrop is in the Barents Sea, where maximum densities reach $\sigma_0 \sim 27.97$ kg m^{-3}. Denser waters have been observed in the Barents Sea: *Schauer et al.* [2002a] reported bottom water in the vicinity of St. Anna Trough as dense as 28.05 kg m^{-3}. Although of high density, these waters mainly ventilate layers of lower density as a consequence of turbulent mixing on exiting the Barents Sea. They contribute to the sub-surface Atlantic Water (AW) layer in the central Arctic Ocean; the core of this layer resides at depths around 500–700 m [e.g., *Carmack*, 2000], and the 0°C isotherm is found at depths ~800 m [*Carmack et al.*, 1997]. Therefore we will assume that potential temperature (heat flux) constraints can be applied to below the density $\sigma_{1.0} > 32.750$ kg m^{-3} (almost equivalent to 28.035 σ_0). This isopycnal surface corresponds to depths greater than ~1,000 m and relevant only, therefore, to Fram Strait and a tiny part of the Storfjordrenna between Bear Island and Svalbard in the BSO.

2.2. Data and Model Output

[17] The inverse model domain is a single box bounded by CTD observations in four major gateways enclosing the Arctic Ocean: Davis, Fram, and Bering Straits and the BSO (see Figure 2). The data used in this study comprise 131 finely spaced hydrographic stations, and 16 GCM grid cells in the BSO which function as CTD stations in regions of absent data. The CTD data were obtained as follows:

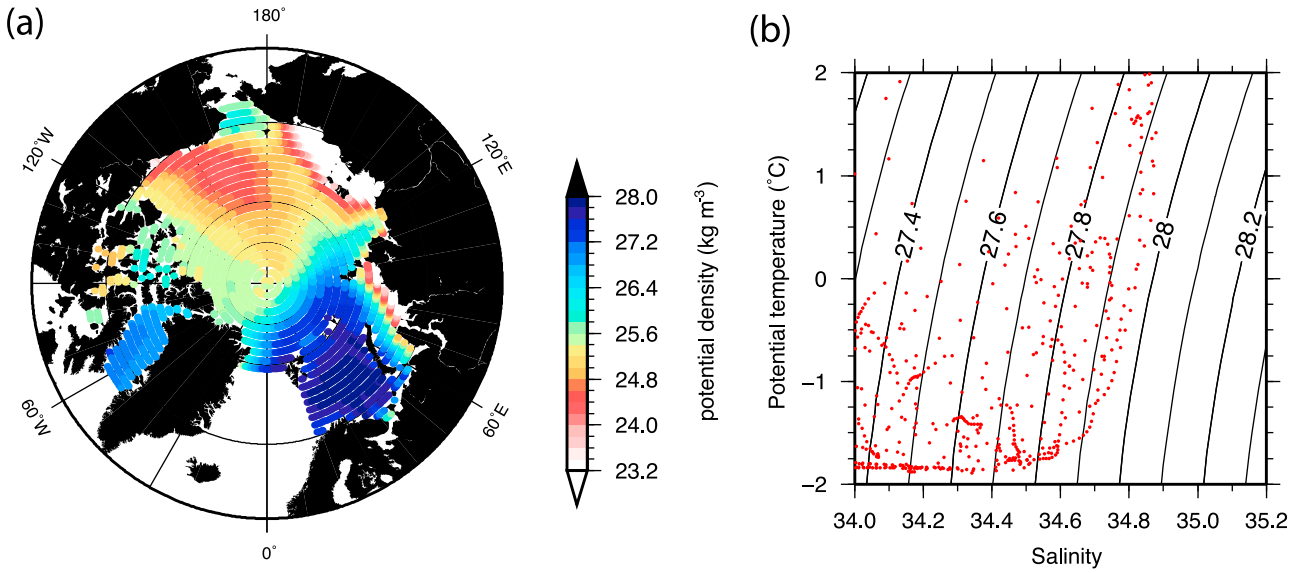

Figure 1. (a) Winter potential density (kg m^{-3}) distribution at 10 m depth based on PHC climatology [*Steele et al.*, 2001]. (b) The θ-S distribution of the data, with density contours overlaid.

16 stations during 5–10 September 2005 in Davis Strait [*Lee et al.*, 2004]; 74 stations during 16 August to 9 September 2005 in Fram Strait [*Fahrbach and Lemke*, 2005]; 29 stations during 9–14 August 2005 in the BSO [*Skagseth et al.*, 2008]; and 12 stations on 21 August 2005 in Bering Strait [*Woodgate et al.*, 2008]. A total of 131 stations were collected within 32 days, between 9 August and 10 September 2005. They span an oceanic distance of 1803 km, comprising 1464 km of measurements supplemented by 340 km of GCM grid points. The total (vertical) section area is 1,050 km^2, of which 1,024 km^2 is covered by measurements and 26 km^2 by the GCM. The (horizontal) surface area of ocean enclosed by the sections is 11.3 $\times$ 10^{12} m^2 [see *Jakobsson*, 2002], with allowance for different definitions of Baffin Bay.

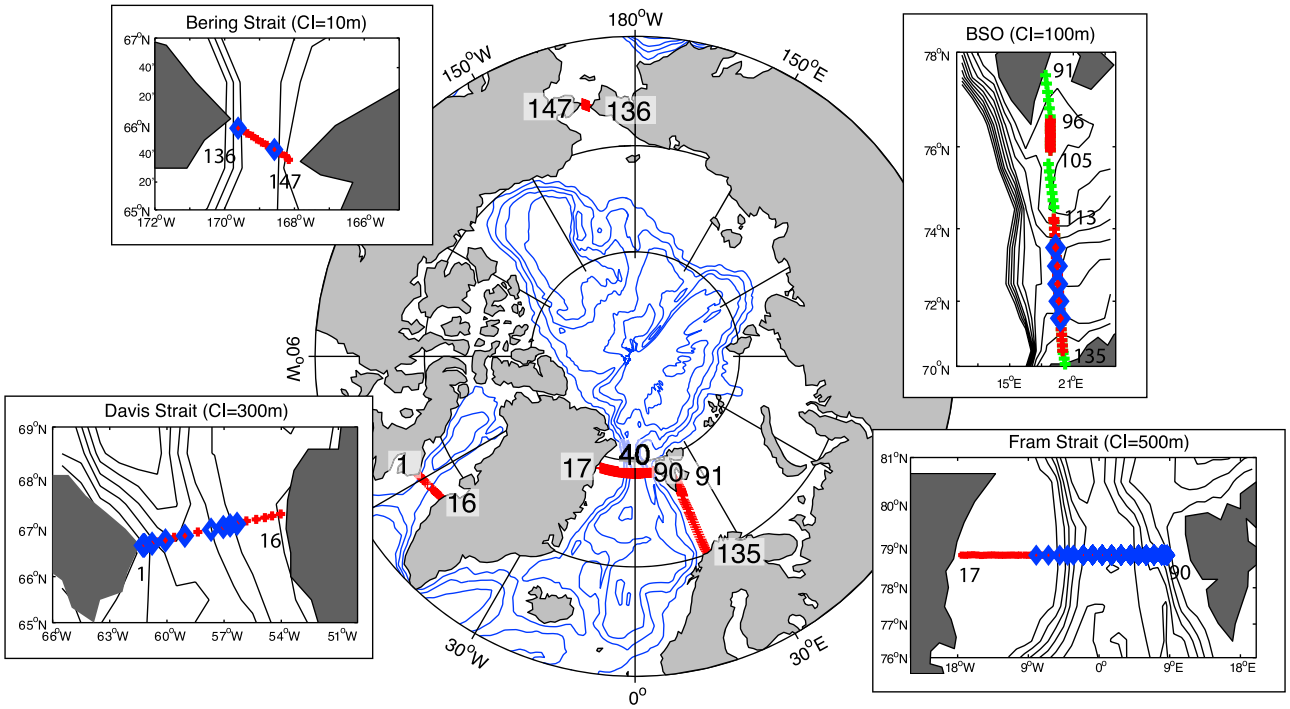

Figure 2. Bathymetric configuration in Davis, Fram, and Bering Straits and the Barents Sea Opening (BSO), showing CTD stations (red cross), OGCM model grid points (green cross), mooring locations (blue diamond), and station numbers (including model grid points). Bathymetric contour intervals (CI) are shown for each strait; the CI for the Arctic figure is 1000 m.

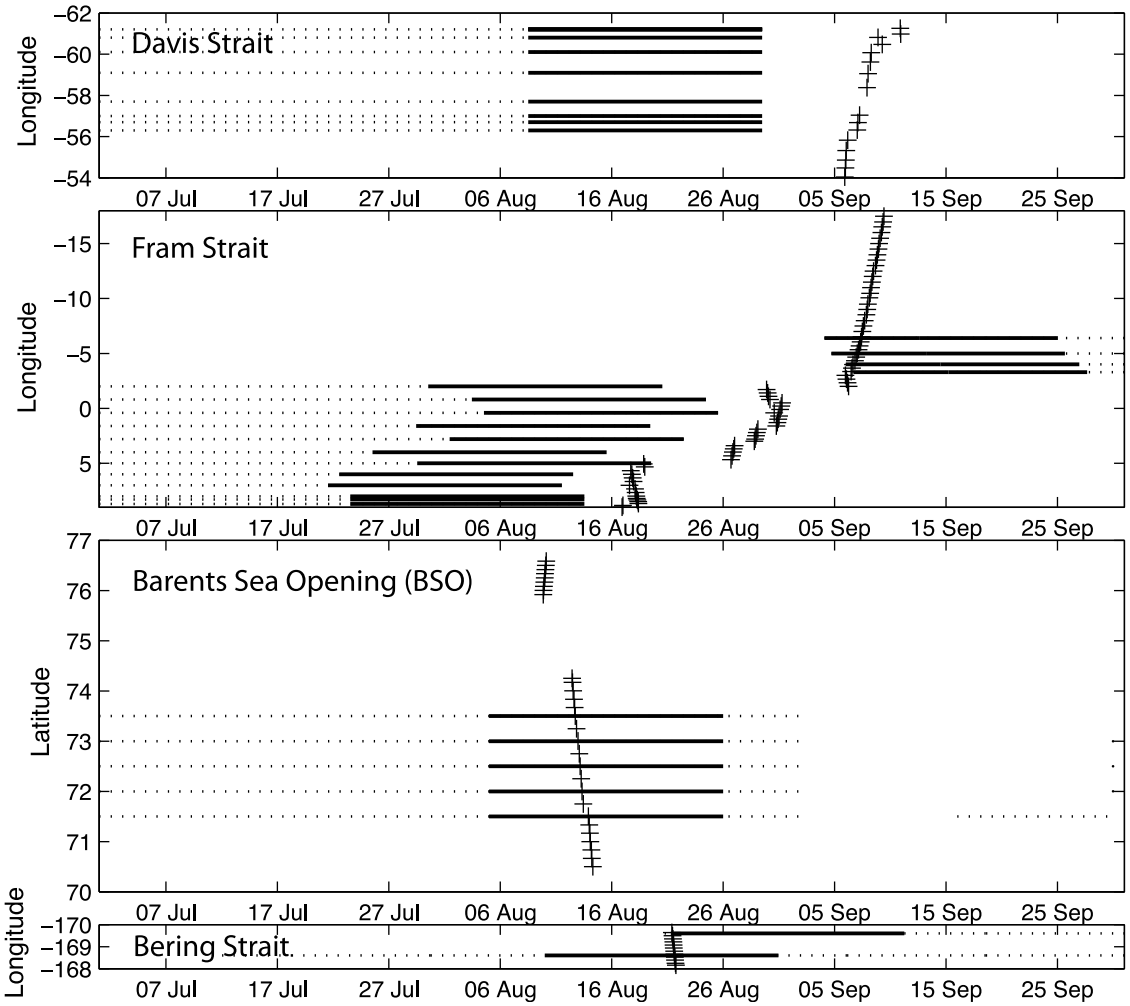

Figure 3. Observational periods of CTD stations and moored current meters in each strait (Davis, Fram, Bering Straits and the BSO). The height of each figure is scaled to the width of each strait. Crosses show the timing of CTD observations in 2005; dotted lines show the observational periods of moored current meters; solid lines show the 3-week averaging period used to obtain initial estimate of reference velocities.

[18] Velocity data from 31 moorings deployed in these straits are used to initialize the reference velocities. The distribution of these moorings is: 4 in western Fram Strait (Norwegian Polar Institute, Tromsø) [*de Steur et al.*, 2009]; 12 in central and eastern Fram Strait (Alfred Wegener Institute, Bremerhaven) [*Schauer et al.*, 2008]; 5 in the BSO (Institute for Marine Research, Bergen) [*Skagseth et al.*, 2008]; 2 in Bering Strait (University of Washington) [*Woodgate et al.*, 2006]. In Davis Strait, weekly averaged optimal interpolation (OI) velocity fields based on temperature, salinity and velocity observations from 8 moorings are used [see *Curry et al.*, 2011]. Over Belgica Bank in the western Fram Strait where moored observations are lacking, vessel-mounted ADCP (VMADCP) data are used [*Fahrbach and Lemke*, 2005]. VMADCP data are collected from the same cruise as the CTD observations in Fram Strait. The timing of the CTD observations and the locations of the moorings around the Arctic boundary are shown in Figure 3.

[19] Model output is used to fill small gaps in the BSO where observations are lacking. The model is an implementation of the Nucleus for European Modeling of the Ocean (NEMO) coupled ice-ocean GCM at NOC, Southampton [*Barnier et al.*, 2006]. The model's global mean spatial resolution is 0.25° but the tripolar grid increases the local (Arctic) resolution to 20 km. Model output is available between January 1958 and December 2007 every 5 days. In this study, we analyze temperature, salinity and velocity output in summer 2005. The hydrographic data gaps on the BSO section lie south of Svalbard, north of Bear Island (74.3°N), and near the Norwegian coast (Figure 2), where 16 NEMO grid points act as substitute CTD stations. We also employ NEMO velocity output as initial velocity estimates where hydrographic data are present but in situ velocity data are absent: for north of Bear Island and south of 71.5°N in the BSO. NEMO has been used successfully in several high-latitude northern-hemisphere analyses, for example: in the Arctic Ocean and Nordic Seas, concerning FW fluxes east and west of Greenland [*Lique et al.*, 2009, 2010; *Marsh et al.*, 2010]; concerning Arctic primary production [*Popova et al.*, 2010]; and concerning North Atlantic ocean heat fluxes [*Grist et al.*, 2010].

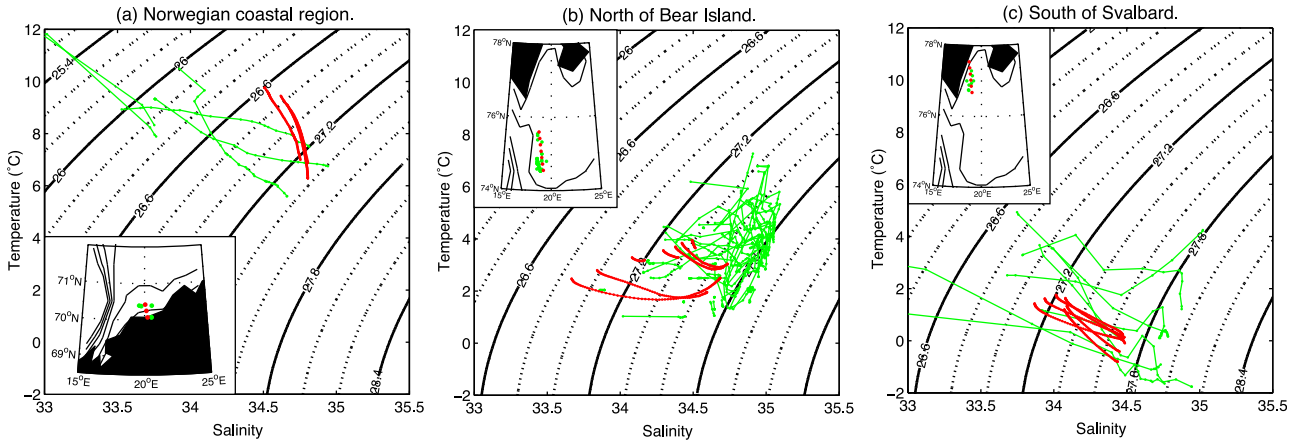

Figure 4. (a) T-S plots of available historical CTD data (green) and NEMO output of temperature and salinity (red) in the Norwegian coastal region along the BSO. Profile locations are shown in the map, which is inserted in the T-S diagram. Bathymetry is also shown with contour interval of 200 m. (b) Same as Figure 4a but for north of Bear Island. (c) Same as Figure 4a but for south of Svalbard.

[20] The NEMO output of temperature and salinity in the relevant areas of the BSO are compared with available historical CTD data from the World Ocean Database 2009 [*Boyer et al.*, 2009] and Hydrobase 2 [*Curry*, 2001], which includes the Barents and Kara Seas Oceanographic Database [*Golubev et al.*, 2000]. All CTD data since 1995 during July–September near the NEMO grid are used (Figure 4). In the Norwegian coastal region, 5 historical CTD profiles are available within 19.0–21.0°E, 70.0–70.4°N. NEMO salinity (34.5–34.7) is systematically higher than CTD data by ∼0.5, while NEMO temperatures lie within the range (6–10°C) of the CTD data [see also *Skagseth et al.*, 2011]. This positive salinity bias in the NEMO representation in the Norwegian Coastal Current (NCC) results from an over-saline simulated outflow from the Skagerrak compared with the hydrography [e.g., *Røed and Albretsen*, 2007]. Therefore, the 3 NEMO salinity profiles in this region are corrected by subtracting 0.5. To the north of Bear Island, 50 historical CTD profiles are available within 18.5–19.5°E, 74.5–75.6°N. NEMO salinities are slightly higher than the historical observations but still fall broadly within the envelope of observed values, while NEMO temperatures show no systematic difference from the CTD data; so no corrections are introduced. To the south of Svalbard, 8 historical CTD profiles are available within 18.0–19.0°E, 76.7–77.6°N. NEMO salinities and temperatures all fall within the range of observations, so no corrections are introduced.

[21] NEMO velocity output in the BSO is compared with the small number of available velocity observations. In the Norwegian coastal region, *Skagseth et al.* [2011] shows the seasonal cycle of velocity during July 2007 to July 2008 observed by bottom-mounted upward-looking ADCPs at 71.1°N, 24.0°E. The NEMO bottom velocity (6 cm s^{-1}) agrees well with their summer mean velocity at 172–188 m (6.6 cm s^{-1}). Between Bear Island and Svalbard, 13 hydrographic and VMADCP sections were occupied during July 1997 to November 1999 [*O'Dwyer et al.*, 2001]. NEMO velocities in this region in the upper 200 m are compared with their results [*O'Dwyer et al.*, 2001, Figure 4]. NEMO velocities associated with the topographic recirculation in Storfjordrenna (3–5 cm s^{-1}) are generally weaker than measured (8–12 cm s^{-1}), but as *O'Dwyer et al.* [2001] observe, the region is shallow and transports are small, so no adjustment is introduced to bottom velocities between Bear Island and Svalbard. The impact of introducing NEMO model output to the inverse model is examined in section 3.5.

[22] The circum-Arctic distributions of potential temperature and salinity are shown in Figure 5. Their (area-weighted) mean values are 1.159°C and 34.662, respectively, where the latter includes the mobile sea ice area with salinity of 6 (see section 2.5). The sub-division of the water column employs density criteria based on *Rudels et al.* [2008]; six layers are selected, which we name Surface, Subsurface, Upper AW, AW, Intermediate Water and Deep Water (Figure 5 and Table 1). Table 1 also includes the further sub-division of these layers for use in the inverse model, which is described in section 2.3; also included in Table 1 are conventional central Arctic Ocean water masses, for reference.

[23] Since water masses are generally defined using potential temperature and salinity classes, there is generally no unique relationship between water masses and the layers defined by density. Also, our naming of layers is admittedly imperfect: for example, the Subsurface and Upper AW layers can be found at the surface, particularly in Fram Strait and the BSO; and the AW layer can include water other than AW. Nevertheless, these are simple and useful categories that capture dominant features. The water masses occupying the circum-Arctic section are next briefly described, for each part of the section, and are illustrated on the θ-S plot (Figure 6).

[24] Bering Strait is shallow (∼50 m depth); it is occupied by fresh (<33), warm (2–8°C) summer Pacific Water (sPacW), and the Alaskan Coastal Current Water (ACCW) is seen on the east side of the strait as warmer (>6°C), fresher (<32) water [*Steele et al.*, 2004; *Woodgate and Aagaard*, 2005]. sPacW occurs in both the Surface and Subsurface layers, while the ACCW is found only in the Surface layer.

[25] In the BSO, warm (3–7°C) and saline (35.0–35.2) AW appears in the middle of the section as a dominant feature, and is found in both Upper AW and AW layers.

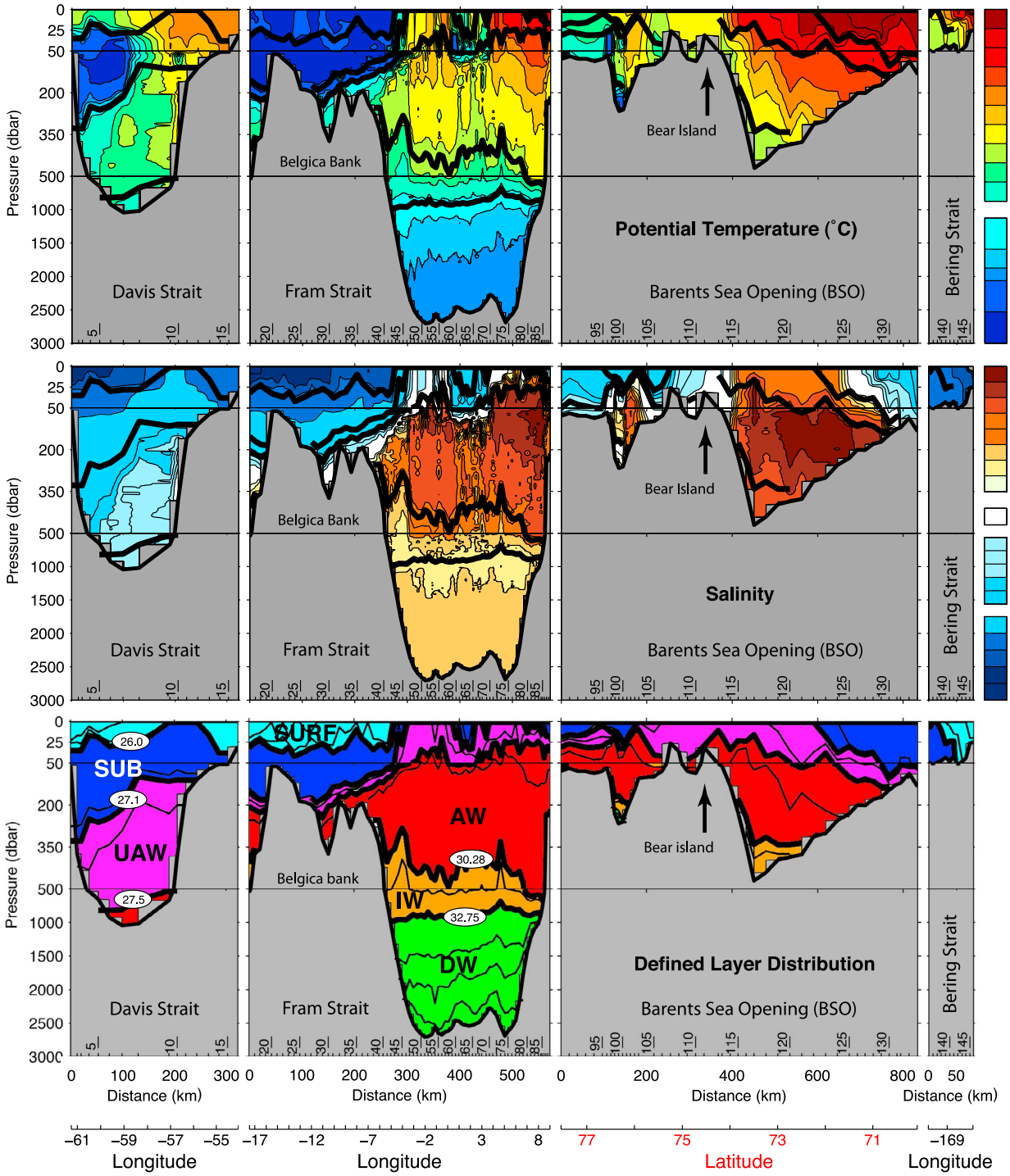

Figure 5. (top) Potential temperature section and (middle) salinity section along Davis and Fram Straits the BSO and Bering Strait; bold black lines show defined water mass boundaries, and the color bar scale is nonlinear. (bottom) The distribution of defined water masses and layer boundaries along the section. These corresponding densities are labeled: 26.0 σ_0, 27.1 σ_0, 27.5 σ_0, 30.28 $\sigma_{0.5}$, and 32.75 $\sigma_{1.0}$. The pressure axis is expanded between 0 and 50 dbar and 50 and 500 dbar and station numbers are shown along the base of each plot.

Table 1. Definitions of Model Layers, Observed Water Masses, and Common Water Masses in the Central Arctic Ocean

Layer	Upper Interface	Lower Interface	Layer Group	Central Arctic[a]	Davis	Fram	BSO	Bering
1	Surface	24.700 σ_0	Surface Water	MLW, UHW	WGSW, SBICW	PSW, PSWw	—	ACCW, sPacW
2	24.700 σ_0	25.500 σ_0						
3	25.500 σ_0	26.000 σ_0						
4	26.000 σ_0	27.000 σ_0	Subsurface Water	UHW, LHW	WGSW, ArcW	PSW, PSWw	NCCW, ESCW	sPacW
5	27.000 σ_0	27.100 σ_0						
6	27.100 σ_0	27.300 σ_0	Upper AW	LHW	WGIW	PSW, PSWs, AW	AW	—
7	27.300 σ_0	27.500 σ_0						
8	27.500 σ_0	27.700 σ_0	AW	AW, ASW, PIW	TrW	AW	AW	—
9	27.700 σ_0	30.280 $\sigma_{0.5}$						
10	30.280 $\sigma_{0.5}$	30.320 $\sigma_{0.5}$	Intermediate Water	UIW, LIW	—	AIW	BSW, BrSW	—
11	30.320 $\sigma_{0.5}$	32.750 $\sigma_{1.0}$						
12	32.750 $\sigma_{1.0}$	35.126 $\sigma_{1.5}$	Deep Water	ADW	—	DW	BSW, BrSW	—
13	35.126 $\sigma_{1.5}$	35.142 $\sigma_{1.5}$						
14	35.142 $\sigma_{1.5}$	37.457 $\sigma_{2.0}$						
15	37.457 $\sigma_{2.0}$	Bottom						

[a]The following definitions are based on *Aksenov et al.* [2010, Table 2, and references therein]: Mixed Layer Water (MLW), Upper Halocline Water (UHW), Lower Halocline Water (LHW), Atlantic Water (AW), Arctic Surface Water (ASW), Polar Intermediate Water (PIW), Upper Intermediate Water (UIW), Lower Intermediate Water (LIW), and Arctic Deep Water (ADW). Absence of a water mass from a density class is denoted by a dash. Abbreviations and references for observed water masses are as follows: Davis Strait [after *Tang et al.*, 2004; *Cuny et al.*, 2005; *Curry et al.*, 2011]: West Greenland Shelf Water (WGSW), Surface Baffin Island Current Water (SBICW), West Greenland Intermediate Water (WGIW), and Transitional Water (TrW); Fram Strait [after *Rudels et al.*, 2002, 2005]: Polar Surface Water (PSW), Polar Surface Water warm (PSWw), Atlantic Water (AW), Arctic Intermediate Water (AIW), and Deep Water (DW); BSO [after *Loeng*, 1991; *Sætre*, 1999; *Furevik*, 2001; *Schauer et al.*, 2002a; *Fer et al.*, 2003; *Ingvaldsen et al.*, 2004]: Norwegian Coastal Current Water (NCCW), East Spitsbergen Current Water (ESCW), Barents Sea Water (BSW), and Brine-enriched Shelf Water (BrSW); and Bering Strait [after *Steele et al.*, 2004; *Woodgate and Aagaard*, 2005]: summer Pacific Water (sPacW) and Alaskan Coastal Current Water (ACCW). Note that SBICW (T > 0. and S < 32) in Davis Strait and ESCW (T > 0. and S < 34.2) in the BSO are named in this study. Absence of a water mass from a density class is denoted by a dash.

Warmer (<8°C) and fresher (34–35) Norwegian Coastal Current Water (NCCW) is present in the southern part of the section in both NEMO grid points and CTD stations, and it appears in the Subsurface layer. Barents Sea Water (BSW) occupies the deepest parts to the south of Bear Island, and is in the Intermediate Water layer. Brine-enriched shelf water (BrSW) at the freezing point temperature appears in the northern part of Storfjordrenna between Bear Island and Svalbard in the Intermediate Water and Deep Water Layers. Finally, the cold, fresh and well-stratified waters between Svalbard and Bear Island appear to lack a conventional name, so we refer to this as East Spitzbergen Current Water (ESCW),

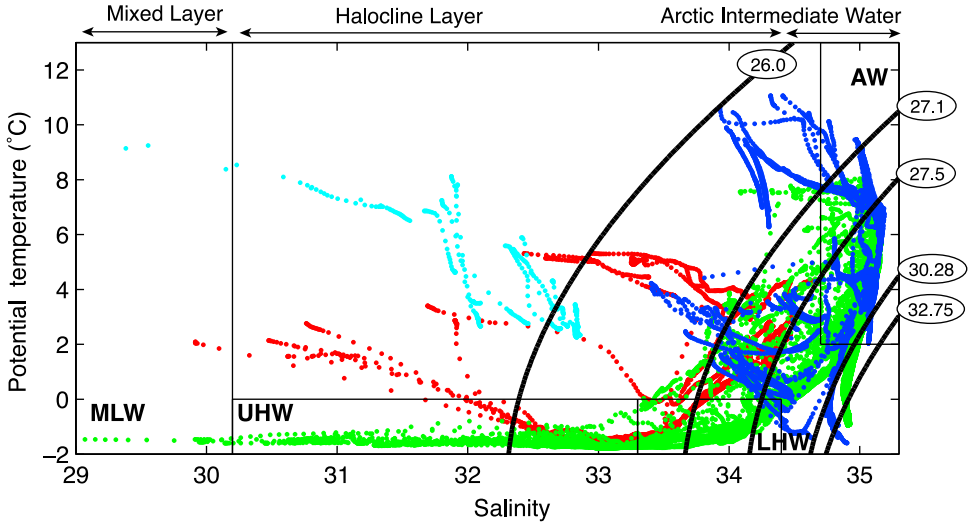

Figure 6. The θ-S plot from all sections; the color code is as follows: Davis Strait is red, Fram Strait is green, BSO is blue, and Bering Strait is cyan. Defined major water mass divisions (density contours) are in black. These corresponding densities are 26.0 σ_0, 27.1 σ_0, 27.5 σ_0, 30.28 $\sigma_{0.5}$, and 32.75 $\sigma_{1.0}$. Some conventional water masses (MLW, UHW, LHW, and AW) and water mass layers (Mixed Layer, Halocline Water, and Arctic Intermediate Water) in the central Arctic are shown based on *Aksenov et al.* [2010, Table 2].

Table 2. A Priori Uncertainties in Volume Conservation and the Mean and Standard Deviation of Potential Temperature and of Salinity Anomaly in Each Layer

Model Layer	Uncertainty (Sv)	Potential Temperature (θ, °C)	Salinity Anomaly
1	4.0	0.716 ± 3.052	−4.097 ± 0.311
2	4.0	0.637 ± 2.859	−3.155 ± 0.403
3	4.0	1.650 ± 2.546	−2.356 ± 0.250
4	4.0	0.822 ± 3.887	−1.331 ± 0.605
5	4.0	2.176 ± 3.633	−0.688 ± 0.421
6	3.0	3.050 ± 3.453	−0.443 ± 0.426
7	3.0	2.426 ± 3.070	−0.265 ± 0.379
8	2.0	3.486 ± 2.612	0.081 ± 0.331
9	2.0	3.396 ± 1.381	0.368 ± 0.208
10	1.0	1.976 ± 0.622	0.325 ± 0.093
11	1.0	0.497 ± 0.617	0.259 ± 0.052
12	0.5	−0.511 ± 0.196	0.245 ± 0.020
13	0.5	−0.783 ± 0.120	0.254 ± 0.015
14	0.5	−0.896 ± 0.105	0.257 ± 0.016
15	0.5	−0.922 ± 0.131	0.263 ± 0.012
Full depth	1.0	1.160 ± 2.673	0.017 ± 0.975

and it occupies three layers (Subsurface, Upper AW, AW) [see *Loeng*, 1991; *Sætre*, 1999; *Furevik*, 2001; *Schauer et al.*, 2002a; *Fer et al.*, 2003; *Ingvaldsen et al.*, 2004].

[26] In Fram Strait, very fresh Polar Surface Waters (PSW; 28–34.5) near the freezing point of seawater appear over Belgica Bank and in the East Greenland Current (EGC); the more saline fraction (∼30–34.5) of these waters resemble Arctic Halocline water, and occupy the Surface and Subsurface layers. The Upper AW layer is very thin; beneath it over Belgica Bank is a water mass in the AW layer that resembles Lower Halocline water. In the EGC, the AW layer contains modes of recirculated and/or returned AW which have arrived there either via the "short circuit," recirculating close north of Fram Strait, or via the longer circuit around the Eurasian Basin. Slightly colder (−0.5 to 2°C) and fresher (∼34.85) water is found in the Intermediate layer, which is likely highly modified AW that has taken the long circuit around the whole Arctic Ocean. The dominant water in the upper layers of eastern Fram Strait is warm (3–6°C) and saline (35.0–35.2) AW in the West Spitzbergen Current (WSC), which is partly overlain by a mixture of Arctic- and Atlantic-sourced waters in the Subsurface layer. The Intermediate layer here contains intermediate waters from the Nordic Sea. The central region of Fram Strait exists between the north-going warm and saline regime to the east and the south-going cold and fresh regime to the west, and as such, it represents a transition region between these two extremes, displaying evidence of transient eddies, quasi-stationary meanders, and substantial local recirculation. Water in Fram Strait deeper than ∼1,000 dbar (in the Deep Water layer) has small ranges of temperature and salinity: −0.7 ± 0.1°C and 34.90 ± 0.01, and contains a mixture of various deep waters sourced from the Nordic Seas and Arctic Ocean [see *Rudels et al.*, 2002, 2005].

[27] Much of Davis Strait is occupied by relatively fresh (<34.5) water. A temperature minimum (close to the freezing temperature) appears in the western part of the strait; it corresponds to Arctic Halocline water, and is found in the Subsurface layer. Warmer water (4–5°C) exists in the eastern part of Davis Strait, possibly reflecting the Atlantic Ocean origin of the West Greenland Current; it is found in the Surface and Subsurface layers. In the Surface layer on the west side is an otherwise unnamed feature of moderate temperature and very low salinity which may be influenced by surface meltwater runoff; we refer to it as Surface Baffin Island Current Water (SBICW). The AW layer contains a relatively warm and saline water mass that has been called West Greenland Intermediate Water (WGIW), although this regional name may not accurately reflect its origins [see *Tang et al.*, 2004; *Cuny et al.*, 2005; *Curry et al.*, 2011].

2.3. Inverse Model Setup

[28] The inverse model used in this study is formulated with 15 layers defined using isopycnal surfaces. Different reference depths are used to calculate potential density depending on the average depth of the surface. Model layers are listed in Table 2. The following constraints are applied to the inverse model: full-depth conservation of volume and salinity anomaly transport (1 constraint each); conservation of volume transport and of salinity anomaly transport for each layer; and conservation of potential temperature anomaly transport in the four deepest layers ($\sigma_{1.0} > 32.750\ \mathrm{kg\,m^{-3}}$; see section 2.1) that do not outcrop in winter. Therefore 36 constraints in total are prescribed. Salinity anomaly and potential temperature anomaly are obtained by subtracting the mean property value around the boundary of the model domain (cf. section 2.1), which improves the conditioning of the inversion [*McIntosh and Rintoul*, 1997; *Ganachaud*, 1999]. The resulting conservation equations for transport T of volume or of some property C are of the general form

$$T_m = \sum_{j=1}^{N} \Delta x_j \int_{h_m}^{h_{m+1}} (v_j + b_j)\, C_j\, dp - (w_m^C \mathcal{A}_m C_m) + (w_{m+1}^C \mathcal{A}_{m+1} C_{m+1}) = 0, \tag{8}$$

where j and m refer to station pair and layer interface indices respectively, N is the total number of station pairs, Δx is the station spacing, h_m and h_{m+1} are the depths of the upper and lower interfaces of model layer m, C is property concentration either around the boundary (C_j) or over an interface (C_m), v is geostrophic velocity calculated from hydrography, b is the barotropic velocity, w_m^C is the effective interfacial velocity for each property C, and $\mathcal{A}_m$ is the layer interface area within the domain. For each layer therefore, the transport T_m of volume or of property C is the sum of the transports through the sides of the layer, and into and out of the upper and lower interfaces. *McIntosh and Rintoul* [1997] and *Sloyan and Rintoul* [2001] showed that property-specific diapycnal velocities across each layer interface are effective parameterizations of net diapycnal fluxes in inverse models.

[29] The first layer is a special case because it receives in the model the net FW input and accommodates the Fram Strait sea ice flux. The model layer 1 transports, T'_1, are

$$T'_1 = T_1 + (uC^{ice}\delta h \delta x) + (A^{surf} q), \tag{9}$$

where the ice is treated as a rectangular plate, C^{ice} is the relevant property concentration, δh is sea ice thickness, δx is the sea ice width, and u is the sea ice advection speed. The

surface input of FW is represented as a transport by the product of a scale area A^{surf} to represent the Arctic Ocean surface area and is set to 10^7 km^2, and a velocity parameter q, which is to be determined.

[30] The depth-independent adjustment to the relative velocity b_j provides 143 unknowns, one for each station pair j. The model includes diapycnal velocities in the ocean interior for each of the 14 layer interfaces for volume and salinity, which provides 28 unknowns, and 4 unknowns are set for potential temperature between the four deepest (non-outcropping) layers. Since potential temperature anomaly conservation is not required for the remaining layers, no diapycnal potential temperature anomaly velocities are derived between them. Sea ice advection velocity u in Fram Strait (1 unknown) and surface FW input q (1 unknown) are included in layer 1 and in the full depth volume and salt anomaly equations. Therefore the model comprises a total of 177 unknowns.

[31] As is conventional, these equations are represented in matrix form

$$\mathbf{Ax} = \mathbf{d}, \tag{10}$$

where $\mathbf{A}$ is M × N and contains information about properties and geometry, $\mathbf{x}$ is N × 1 and contains unknown barotropic, diapycnal, sea ice and FW velocities, and $\mathbf{d}$ is M × 1 and contains initial estimates of transports; M is the number of conservation equations (36), and N is the number of unknowns (177).

2.4. Weighting and Uncertainties

[32] Row and column weighting are applied to the model before inversion to weight constraints and unknowns (respectively), using the row weighting matrix $\mathbf{W}$ (M × M) and column weighting matrix $\mathbf{E}$ (N × N)

$$(\mathbf{WAE})(\mathbf{E^{-1}x}) = (\mathbf{Wd}). \tag{11}$$

The weighted system of equations $\mathbf{A'x'} = \mathbf{d'}$ is then solved using singular value decomposition [*Wunsch*, 1996] with $\mathbf{A'} = \mathbf{WAE}$, $\mathbf{x'} = \mathbf{E^{-1}x}$ and $\mathbf{d'} = \mathbf{Wd}$. $\mathbf{W}$ and $\mathbf{E}$ contain only diagonal components. For volume conservation,

$$W_{mm} = \frac{1}{\varepsilon_m}, \tag{12}$$

where ε_m is the a priori volume transport uncertainty for each layer, and for property transports,

$$W_{mm} = \frac{1}{2\eta_m^C \varepsilon_m}, \tag{13}$$

where η_m^C is the standard deviation of property variations within the relevant layer. All uncertainties and standard deviations are listed in Table 2. The factor 2 in (13) is set according to *Ganachaud and Wunsch* [2000]; it is an ad hoc best guess to account for possible correlations between the section averaged and mesoscale components of the noise in property conservation equations. The weighting term for full-depth salinity anomaly transport conservation is set 4 times larger than (13) to account for the higher standard deviation of full-depth salinity anomaly (0.98) compared with either the AW layer (0.21–0.33) or the IW layer (0.05–0.09).

[33] Column weighting employs a priori uncertainties for all unknowns: for barotropic, diapycnal, sea ice and surface FW velocities (δb, δw, δu and δq),

$$E_{jj} = \left[\delta b_j / A_j\right]^{1/2}, \tag{14}$$

$$E_{jj} = \left[\delta w_j / \mathcal{A}_j\right]^{1/2}, \tag{15}$$

$$E_{jj} = \left[\delta u / (A^{ice}\{\bar{S} - S^{ice}\})\right]^{1/2}, \tag{16}$$

$$E_{jj} = \left[\delta q / A^{surf}\bar{S}\right]^{1/2}. \tag{17}$$

A_j means station pair area for reference velocity, $\mathcal{A}_j$ layer interface area for diapycnal velocity, A^{ice} mobile sea ice cross-sectional area in Fram Strait. $\bar{S}$ is section mean salinity as before. Use of station pair area and layer interface area is normal for the column norms for the reference and diapycnal velocities (respectively). However, for the sea ice advection term, the salinity anomaly of sea ice is ~30, so we employ $A^{ice}(\bar{S} - S^{ice})$ as a representative column norm for sea ice velocity. Similarly, the surface FW input term is normalized by $A^{surf}\bar{S}$.

[34] The a priori uncertainty in the reference velocity is estimated as the standard deviation of moored velocity data over 3 months (0.02–0.05 m s^{-1}). The uncertainties are linearly interpolated onto each station pair as appropriate. In the case of Belgica Bank and in the BSO, larger a priori uncertainties are provided (0.06 m s^{-1}) where direct measurements are lacking. Smaller a priori uncertainties (0.02 m s^{-1}) are provided for Bering Strait to take account of the observation that the flux "first guesses" are similar to the estimation of *Woodgate et al.* [2005], which is based on long-term sustained observations. The a priori uncertainty in the diapycnal velocities is set as 1×10^{-5} m s^{-1}, near the upper end of the range of vertical velocities inferred from observed ocean mixing rates. The a priori uncertainty in the sea ice advection velocity (u) is set to 50% magnitude of its initial estimate. The a priori uncertainty of the total surface FW flux velocity parameter (q) is set to 50% magnitude of its initial estimate.

[35] The a posteriori uncertainties are calculated as the square root of the diagonal component of the error covariance matrix $\mathbf{P}$, which is estimated using the Gauss-Markov formalism [*Wunsch*, 1996]

$$\mathbf{P} = \mathbf{E} - \mathbf{EA^T}(\mathbf{AEA^T} + \mathbf{W})^{-1}\mathbf{AE}. \tag{18}$$

2.5. Inverse Model Velocity Initialization

[36] The initial state of the model must be specified. At the position of each station pair, the reference velocity is initialized from the deepest available moored velocity measurement, from the VMADCP data over Belgica Bank, or from NEMO model grid cells in parts of the BSO. The cross-sectional moored velocity components are averaged over 3 weeks in order to eliminate higher frequency variability. The moorings are spaced more widely than the stations, so

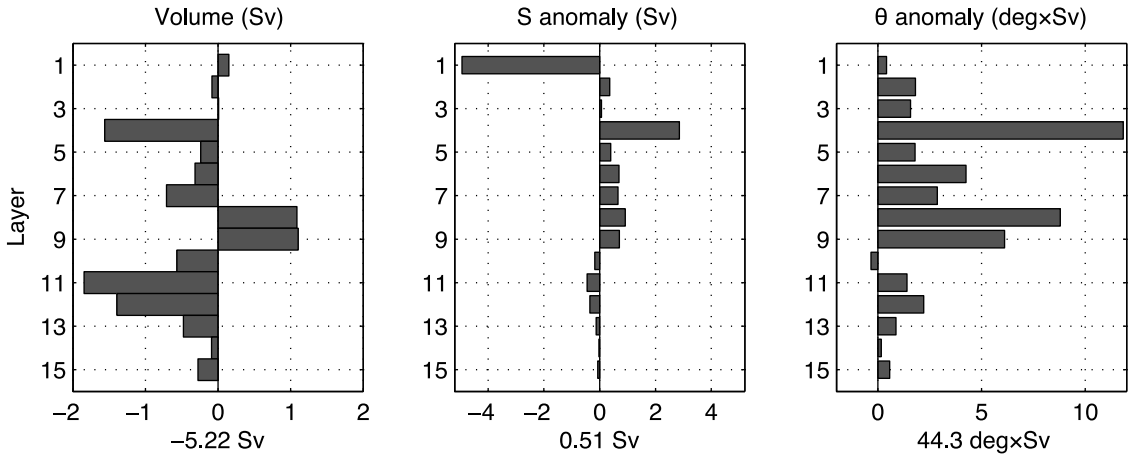

Figure 7. Initial imbalances for (left) volume transport, (middle) salinity anomaly transport, and (right) potential temperature (θ) anomaly transport for each model layer. The total initial imbalances for these parameters are shown beneath each figure.

average velocities are then linearly interpolated onto station pair locations.

[37] Ideally, the 3 week averaging period would center on the hydrographic observations, but in practice the period depends on data availability because the time of the hydrographic observation is also the time when moorings were recovered and replaced. Therefore the averaging period is selected to be as close as possible to the date of the hydrographic observations near each mooring (Figure 3). In Davis Strait, the averaging period is 8–29 August 2005, just before the hydrographic observations (5–10 September). In western Fram Strait, the 3 week averaging period spans 4–27 September depending on the data availability of each mooring, just after the hydrographic observation. In eastern Fram Strait, the 3 week averaging period is just before the hydrographic observations, spanning 21 July to 24 August. In the BSO, the averaging periods are 5–26 August 2005, during the hydrographic observations (9–14 August). In Bering Strait, the averaging periods are 21 August–11 September (just after hydrographic observations) and 10–30 August (during hydrographic observations). NEMO velocities are averaged over 20 days because the output is recorded as 5-day means. The averaging period in the BSO is 3–23 August, which sits in the middle of the hydrographic observations.

[38] All diapycnal velocities are initialized to zero. The area, mean potential temperature and mean salinity of each layer interface in the interior of the Arctic are extracted from the PHC summer data set.

[39] In Fram Strait, the initial sea ice volume flux is set at 50.2 mSv, with salinity anomaly flux of 1.44 Sv, equivalent to 41.5 mSv FW flux. These are calculated as follows. The zonal extent of mobile sea ice is taken to lie between 12 and 3°W. There is a stationary region of fast ice between the Greenland coast and 12°W. The eastern edge of 3°W is selected as a simple version of the sea ice thickness parameterization of *Kwok* [2004]. The mean sea ice thickness of 1.8 m is as observed by upward-looking sonar (ULS) in August 2005 at 5°W (E. Hansen, Thinning of Arctic multiyear and ridged sea ice 1990–2010, manuscript in preparation, 2012). Sea ice salinity is set to 6. Summer 2005 is a difficult time to estimate sea ice volume flux. This year featured widespread change in thickness composition [*Kwok*, 2007; *Nghiem et al.*, 2007] and a peak in the Fram Strait sea ice export [*Kwok*, 2007]. We focus on August and September (AS) 2005 and estimate its sea ice volume flux during the period when the hydrographic observations were conducted. *Kwok* [2004] estimated sea ice volume flux of four summer months (JJAS) during 1991–1999 as 30.6 $\pm$ 7.8 mSv with sea ice area flux of 115 $\pm$ 20 $\times$ 10^3 km^2 (over JJAS) based on the sea level pressure gradient across Fram Strait, and a thickness parameterization based on ULS sea ice thickness observations [*Vinje et al.*, 1998]. Based on the pressure gradient, *Kwok* [2007] also estimated sea ice area fluxes of 140 $\times$ 10^3 km^2 over 4 months (JJAS) during 2000–2006 and 250 $\times$ 10^3 km^2 over 4 months (JJAS) in 2005, with a large area flux estimation of 180 $\times$ 10^3 km^2 over 2 months, AS 2005. Hansen (manuscript in preparation, 2012) has shown significant sea ice thickness reduction from the 1990s of 3.3 $\pm$ 0.5 m to the 2000s of 2.2 $\pm$ 0.6 m, including 1.8 m in August 2005 based on ULS observations. Combining the *Kwok* [2007] sea ice area flux estimate and the Hansen (manuscript in preparation, 2012) sea ice thickness measurement, the sea ice volume flux estimate for the four summer (JJAS) months in 2000–2006 is 23.9 mSv, for the four summer (JJAS) months 2005 is 34.9 mSv, and for AS 2005 is 50.2 mSv. We employ 50.2 mSv as the initial sea ice volume flux estimate for our inversion, which requires therefore a mean advection velocity of 0.15 m s^{-1}.

[40] The initial total surface FW input is 180 mSv. River runoff of 100 mSv and the excess of precipitation over evaporation of 65 mSv are obtained from *Serreze et al.* [2006]. Baffin Bay total FW input of 15 mSv comprises a component of Greenland ice sheet melt (7 mSv) [*Mernild et al.*, 2009], Canadian Arctic Archipelago ice advection (5 mSv) [*Agnew et al.*, 2008; *Kwok*, 2006] and Baffin Island runoff (3 mSv) (*Canadian Climate and Data Information Archive*: http://climate.weatheroffice.gc.ca/).

[41] Figure 7 shows initial volume, salinity anomaly and potential temperature anomaly transport imbalances for each layer. The net initial imbalances are: volume, 5.22 Sv deficit;

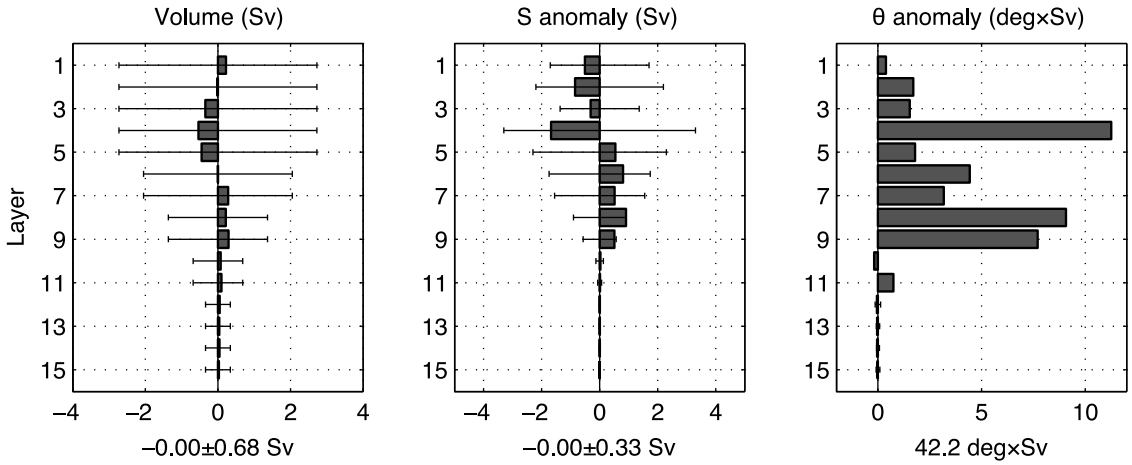

Figure 8. Residual imbalances for (left) volume transport, (middle) salinity anomaly transport, and (right) potential temperature (θ) anomaly transport for each model layer. The total residual imbalances for these parameters are shown beneath each figure. The error bars show 1 standard deviation of the defined a priori error for each layer.

salinity anomaly, 0.51 Sv excess (equivalent to 15 mSv FW deficit); and potential temperature anomaly, 44.3°C × Sv.

3. Results

3.1. Standard Solution

[42] The row- and column-weighted system of equations is solved by singular value decomposition [*Wunsch*, 1996]. A first model run produces a "standard solution" using all available information and the defined layer configuration. Flux calculations require a closed mass budget, so (small) residuals to the standard solution are eliminated by a second model run with two constraints only: full-depth volume and salinity conservation applied to horizontal reference velocities only. The rank of the standard solution (28 out of 36 equations) is selected to yield a dynamically acceptable solution in which perturbations to the initial estimates of the unknowns remain within a priori uncertainties. Residual imbalances for volume, salinity anomaly and potential temperature transports in defined model layers are indistinguishable from zero within one a priori standard deviation (Figure 8). The inverse solutions are quite similar between ranks 21–30. The reference velocities in the standard solution are modified by mean (peak) perturbations of 0.006 (0.02) m s^{-1}. The largest adjustments are introduced over Belgica Bank in Fram Strait. The diagnosed diapycnal volume velocities have a median magnitude of 1–3 × 10^{-7} m s^{-1}. Adjustment to sea ice advection is 0.004 m s^{-1}, equivalent to 2 mSv FW flux. Adjustment to surface FW input is 7 mSv. The residual full-depth volume and salinity flux imbalances from the first model run are small: 0.20 Sv deficit for volume and 0.02 Sv deficit for salinity (equivalent to 0.6 mSv FW excess). They are completely closed by the second inverse model run, which produces very small adjustments for reference velocities only, with mean perturbation of 0.0002 m s^{-1}.

[43] Even though the final full-depth salinity anomaly transport residual is zero, salinity anomaly imbalances still remain in each model layer within layers 1–9, of order 0.5 Sv, equivalent to 14.4 mSv FW. This arises from the larger a priori uncertainty resulting from the larger salinity standard deviation in these layers, and the possible implications of this internal non-conservation will be discussed.

3.2. Horizontal and Vertical Volume Transport

[44] The structure of the geostrophic velocity field, the a priori and a posteriori reference velocity uncertainties, and the associated full-depth and layer-specific volume transports are shown in Figure 9. Transport uncertainties are calculated from the a posteriori reference current uncertainties except in Bering Strait; they are little reduced from the a priori uncertainties (Figure 9a), indicating that our a priori estimates for this parameter were fair. Transport uncertainties in Bering Strait are estimated as the standard deviation of moored velocity data over 3 months, instead of using the small a priori uncertainty employed in the inverse model. We next describe the computed transports and compare our results with previous observations. In order, we consider Davis Strait, Fram Strait, the BSO, and Bering Strait. Table 3 summarizes the obtained net volume transport, FW transport and heat transport in this study.

[45] In Davis Strait, the net export of 3.1 ± 0.7 Sv is mainly due to the Baffin Island Current (4.0 ± 0.5 Sv) which is partly offset by the north going continuation of the West Greenland Current (0.9 ± 0.5 Sv). *Curry et al.* [2011] show the annual cycle of total volume transport in Davis Strait based on moored current, temperature and salinity data in 2004–2005. Our estimate is within the ranges of their August and September volume transports of 3.0 and 2.0 (±1.0) Sv (respectively).

[46] In Fram Strait, over Belgica Bank, west of 6.5°W, we find an anti-cyclonic recirculation with 1.8 Sv northward transport on the west side and 2.1 Sv southwards transport to the east, a net southward export of 0.4 ± 0.6 Sv with characteristic velocities *ca.* 0.1 m s^{-1}, which is lower than moored current meter observations between summer 1999 and summer 2000 in the north of Belgica Bank of 0.27–0.94 m s^{-1} [*Topp and Johnson*, 1997], but note that the inverse model solution makes little change (*ca.* 1 cm s^{-1}) to the observed velocities.

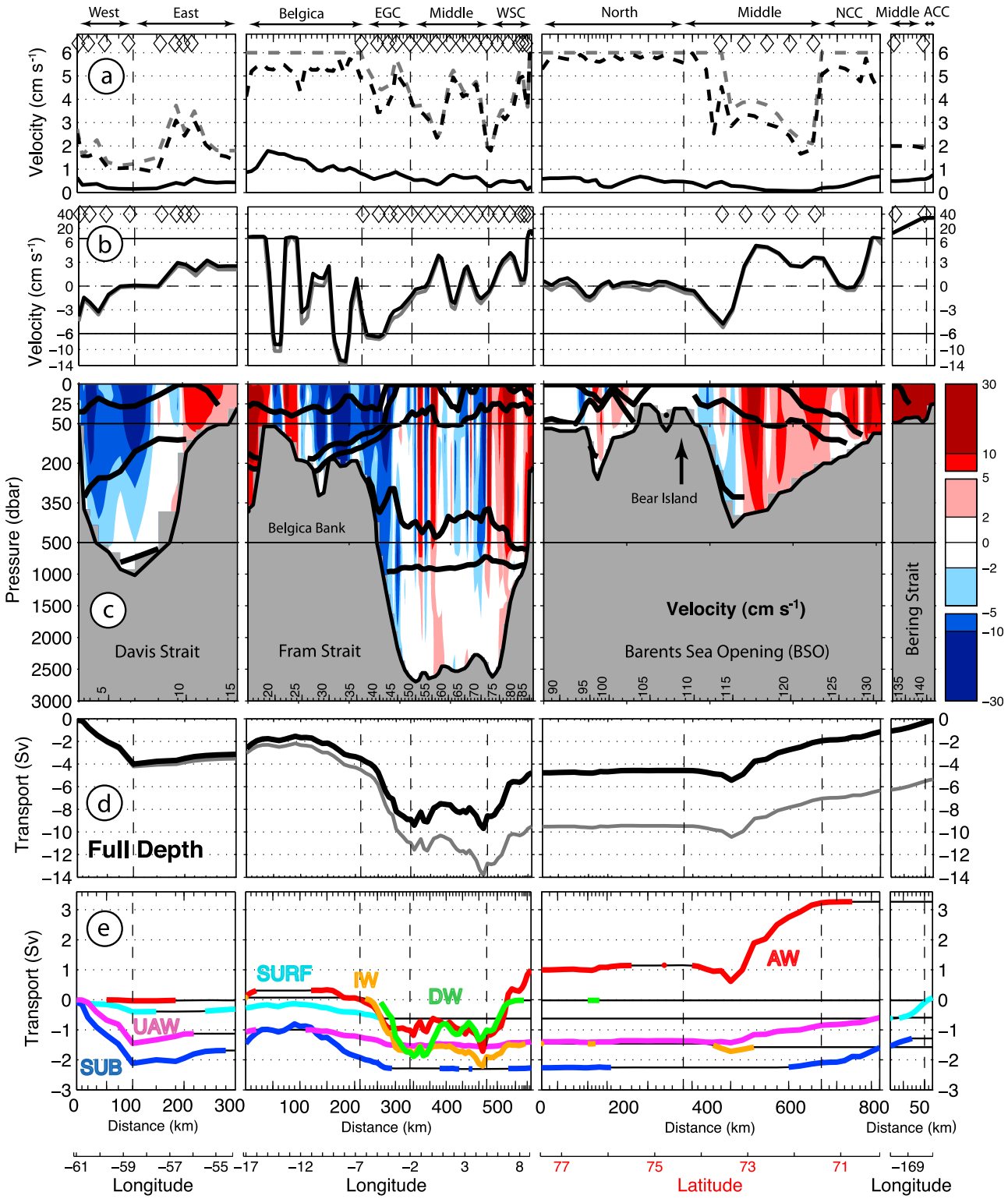

Figure 9. (a) Standard solution for reference velocities (black solid line), defined a priori error for reference velocities (gray dotted line) and a posteriori error for reference velocities (black dotted line) along the section; mooring locations are shown as diamonds. (b) Initial (gray) and final (black) bottom velocities (note change of vertical scale at ± 6 cm s^{-1}); mooring locations are shown as diamonds. (c) Final velocity section (cm s^{-1}); bold black lines show defined water mass boundaries, and red (blue) colors show inflow to (outflow from) the Arctic. (d) Initial (gray) and final (black) full-depth volume transport (Sv) accumulated around the boundary. (e) Accumulated volume transport for each water mass; where a specific water mass is absent from the section, the accumulated transport is plotted as a black line.

Table 3. Summary of Obtained Net Volume, Heat, and FW Transports in Each Main Gateway (Davis, Fram, and Bering Straits and the BSO) and Their Components

Location	Components	Volume Transport (Sv)	FW Transport (mSv)	Heat Transport (TW)
Davis Strait	West of 58°W	−4.0 ± 0.5	144 ± 12	19 ± 2
	East of 58°W	0.9 ± 0.5	−25 ± 8	9 ± 3
	Total	−3.1 ± 0.7	119 ± 14	28 ± 3
Fram Strait	Belgica Bank (west of 6.5°W)	−0.4 ± 0.6	23 ± 23	5 ± 6
	Sea ice	−0.05 ± 0.02	40 ± 14	19 ± 5
	EGC (6.5°W–2°W)	−5.4 ± 2.1	3 ± 16	18 ± 8
	Middle (2°W–5°E)	0.3 ± 3.0	5 ± 22	−6 ± 12
	WSC (east of 5°E)	3.8 ± 1.3	38 ± 12	25 ± 5
	Total	−1.6 ± 3.9	110 ± 40	62 ± 17
BSO	North (north of Bear Island)	0.2 ± 0.5	0 ± 3	2 ± 3
	Middle (71.4°N to Bear Island)	2.6 ± 0.9	36 ± 12	61 ± 15
	NCC (south of 71.4°N)	0.8 ± 0.4	−6 ± 3	23 ± 11
	Total	3.6 ± 1.1	31 ± 13	86 ± 19
Bering Strait	Main (west of 168.4°W)	0.8 ± 0.2	−55 ± 13	9 ± 2
	ACC (east of 168.4°W)	0.2 ± 0.1	−17 ± 6	4 ± 1
	Total	1.0 ± 0.2	−72 ± 14	13 ± 2
All	Total	−0.19 ± 4.13	187 ± 44	189 ± 26

[47] In the EGC region, between 6.5 and 2.0°W, we find 5.4 ± 2.1 Sv export, including 1.7 Sv export in the Deep Water layer. *De Steur et al.* [2009] show the annual cycle of EGC volume transport (between 6.5°W–0.0°E) based on a decade of mooring observations (1998–2008). Their August and September mean volume transports of 4.5 and 6.0 (±2.0) Sv (respectively) are similar to our estimate. The middle of Fram Strait (between 2.0°W–5.0°E) contains a complex velocity structure [cf. *Fahrbach et al.*, 2001; *Schauer et al.*, 2008], where mutually compensating (eddying/recirculating) total northward (4.5 Sv) and southward (4.2 Sv) flows result in a small net southward flow with a large uncertainty (0.3 ± 3.0 Sv), which includes 0.7 Sv northward transport in the Deep Water layer.

[48] In the WSC region (east of 5.0°E), 3.8 ± 1.3 Sv net northward transport is obtained, including 1.0 Sv in the Deep Water layer. *Schauer et al.* [2004] showed volume transport between 3.0 and 4.0 Sv in the WSC region based on mooring observations between 1997 and 2000. Although uniformly northward velocity is seen in the WSC mean velocity field [*Schauer et al.*, 2008], a substantial southward velocity is observed by the moored current meters at 8°E during summer 2005. The time series shows that a stable northward flow of 0.06 ± 0.03 m s^{-1} from 11 May to 26 June becomes a southwards flow of 0.04 ± 0.03 m s^{-1} from 27 June to 16 August, just before the CTD observations. This feature is well captured by the VMADCP during the 2005 cruise that collected the present CTD data, appearing in the same region with the same magnitude. Since the WSC is typically viewed as consistently northward-flowing entity, we inspected the NEMO output for comparable behavior. Similar features were found, as part of continuously westward-propagating eddies, from west of Spitsbergen to around 0°E, with advection speeds of 0.01–0.02 m s^{-1}. Figure 10 shows the initial velocity field compared to a NEMO model 5-day mean velocity field (21–25 August 2005 model time) in this WSC region.

[49] Fram Strait net volume transport is 1.6 ± 3.9 Sv southwards, similar to the long-term moored observation estimate of 2.0 ± 2.7 Sv southwards [*Schauer et al.*, 2008].

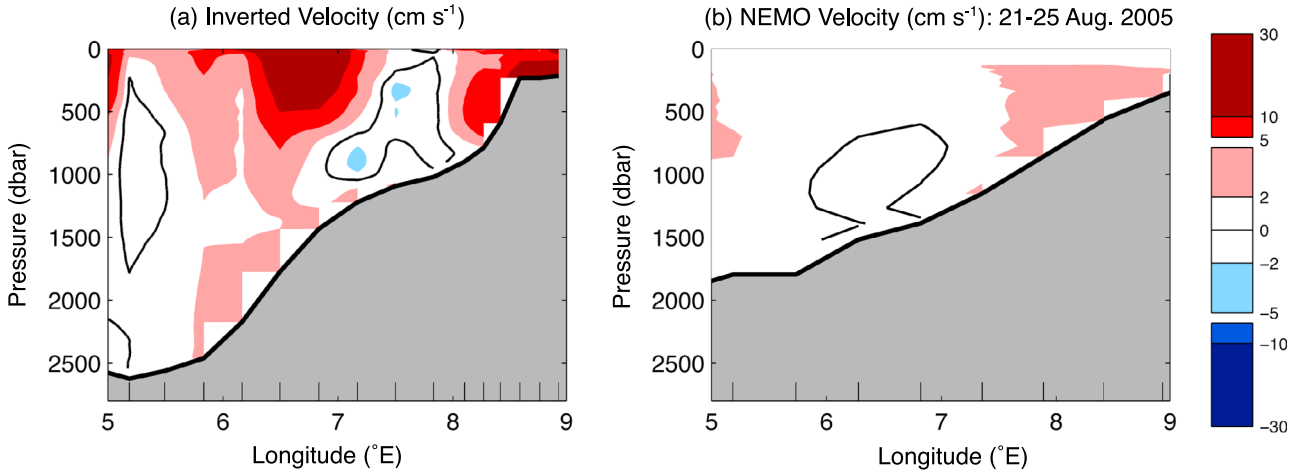

Figure 10. (a) Inverted velocity section in the West Spitzbergen Current region in Fram Strait (cm s^{-1}), with the zero velocity contour shown in black. (b) NEMO model 5-day average velocity field (cm s^{-1}) along 78–79°N zonal model grid line on 21–25 August 2005 model year.

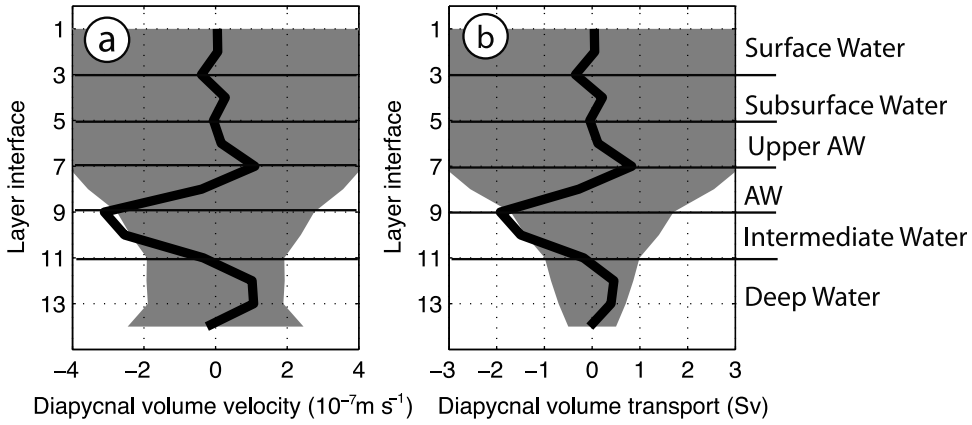

Figure 11. (a) Interior diapycnal volume velocity (10^{-7} m s^{-1}) and (b) associated diapycnal volume transport (Sv). Positive velocity or transport is directed upward. The defined water masses boundaries are labeled. The a posteriori uncertainty is shown by gray shading.

[50] In the BSO, the net inflow is 3.6 ± 1.1 Sv, comprising 0.8 ± 0.4 Sv in the NCC (south of 71.4°N), 3.5 ± 0.8 Sv AW inflow and 0.9 ± 0.6 Sv outflow south of Bear Island in the middle of the section between 71.4°N and Bear Island, and 0.2 ± 0.5 Sv inflow between Bear Island and Svalbard. The NCC region is defined by salinity <34.7 [*Skagseth et al.*, 2008]. The most recent annual-average BSO net volume transport estimate is 2.0 Sv [*Smedsrud et al.*, 2010]. This consists of 1.2 Sv NCC inflow [*Skagseth et al.*, 2011], 2.0 Sv AW inflow in the middle of the section [*Ingvaldsen et al.*, 2002, 2004; *Skagseth et al.*, 2008], 0.9 Sv outflow in the Bear Island Trough [*Skagseth et al.*, 2008] and 0.3 Sv outflow in the shallow Bear Island Current [*Blindheim*, 1989] and zero net flow between Bear Island and Svalbard [*O'Dwyer et al.*, 2001]. Therefore the difference between our estimates and theirs mainly stems from our higher AW inflow in the middle of the section by 1.5 Sv. Our outflow estimates south of Bear Island and NCC inflow are both weaker than theirs by 0.3 Sv and 0.4 Sv, respectively.

[51] In Bering Strait, 0.3 m s^{-1} mean inflow velocity and 1.0 ± 0.2 Sv transport are obtained. The volume transport uncertainty based on the 3-month standard deviation of moored current meter velocity is 0.2 Sv. These values are consistent with the long-term mean inflow of 1.0 Sv in August and 0.7 Sv in September [*Woodgate et al.*, 2005].

[52] In summary, the Deep Water layer in Fram Strait shows a recirculation of 1.7 Sv southwards flow beneath the EGC, in near-balance with northward transports of 0.7 Sv in the central strait region plus 1.0 Sv beneath the WSC. Above the Deep Water layer, shallower than ~1,000 m, the total Arctic Ocean inflow is 9.2 Sv and outflow is 9.3 Sv. The total accumulated ocean volume transport around the Arctic Ocean boundary is 0.14 Sv deficit, balanced by a surface FW input of 0.19 Sv (see section 3.3 below) and sea ice export in Fram Strait of 0.05 Sv.

[53] We next consider vertical volume fluxes (Figure 11). The a posteriori uncertainty is (2–6) × 10^{-7} m s^{-1}, which is much reduced from the a priori uncertainty (1 × 10^{-5} m s^{-1}). The dominant diapycnal velocities and transports concern the AW layer. The accumulated isopycnal AW volume transport across the whole section shows a 3.3 ± 1.1 Sv convergence that is balanced by diapycnal export to adjacent layers. The inverse solution shows (1.1 ± 4.1) × 10^{-7} m s^{-1} upward velocity across the upper AW surface and (3.1 ± 2.8) × 10^{-7} m s^{-1} downward velocity across the lower AW surface, equivalent to exports of 0.8 ± 3.1 Sv upwards through its upper surface into the Upper AW layer, and 1.9 ± 1.7 Sv downward through its lower surface into the Intermediate Water layer, thus expressing the modification of water masses between import and export. While there are some small diapycnal transports within the major layers (between the model water-class layers), all other transports between the major layers are within a posteriori uncertainties. Only downward transport through lower surface of AW into the Intermediate Water layer is statistically significant.

[54] Figure 12 summarizes the Arctic Ocean oceanic volume budget, which shows, for each water mass class, the total inflow, total outflow, net divergence/convergence (i.e., net diapycnal flux), and the residual flux, which is the sum of these three terms. These layer-specific residual volume fluxes are small, but nonzero because volume conservation in each layer is constrained within an a priori error. However, residual volume fluxes sum to zero over all layers as perfect conservation of full-depth volume has been imposed. The central AW layer inputs to the Arctic Ocean a total of 7.2 ± 0.8 Sv, divided between 4.4 Sv from Fram Strait, and 2.9 Sv from the BSO. Fram Strait export (3.4 Sv) is also mainly responsible for the total export (4.0 ± 0.7 Sv) of AW. The remaining 2.8 Sv of AW are transported diapycnally within the Arctic Ocean into adjacent layers, in which they are exported from the Arctic Ocean: 1.9 ± 1.7 Sv descends into the Intermediate layer, 0.8 ± 3.1 Sv ascends into the Upper AW layer, illustrating the extent to which AW is the dominant external oceanic input to the Arctic Ocean.

3.3. Freshwater Flux

[55] In section 2 we derived the expression to calculate FW flux from mass and salinity balance equations, and this shows the role played in FW flux calculation by the section-mean salinity, which is analogous to the "traditional" use of a reference salinity in unbalanced calculations. Figure 13 shows the FW flux section; the area-weighted mean salinity is 34.662, including the mobile sea ice area, with salinity

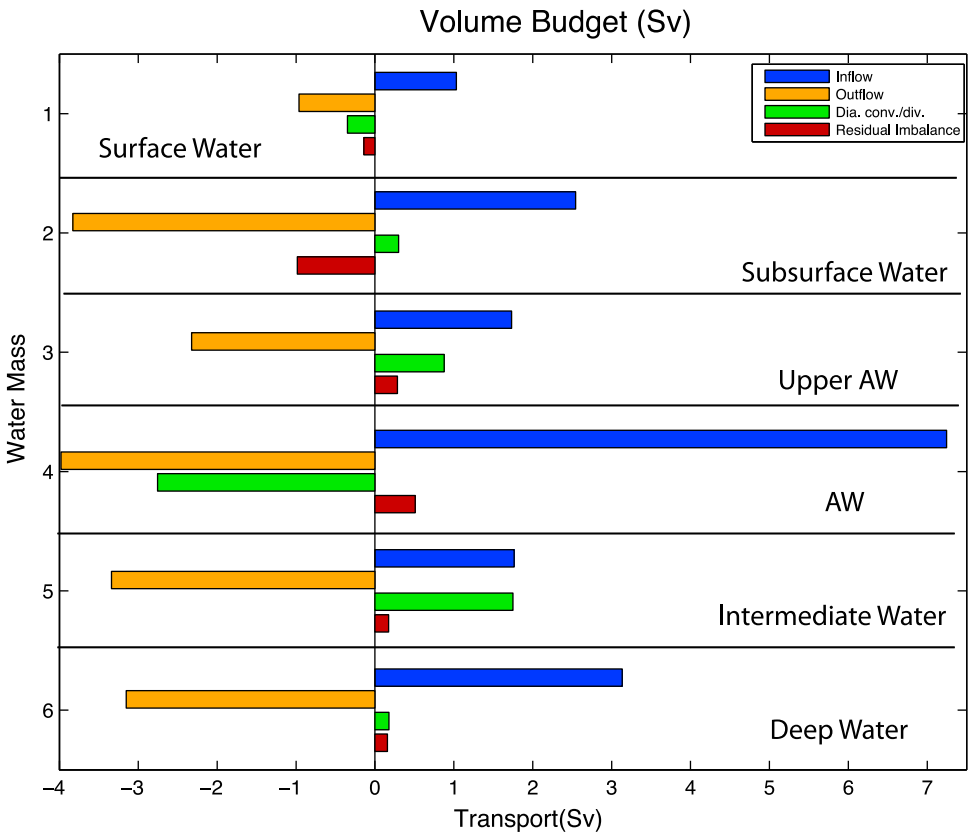

Figure 12. Volume budget (Sv) for each water mass, showing isopycnal inflow (blue), isopycnal outflow (orange), diapycnal convergence/divergence (green), and residual imbalance (red). For each layer, the residual transport is the sum of the other three components. For all layers, the residuals sum to zero.

of 6. The main positive contributions to the calculated surface FW flux arise from saline anomalies entering and fresh anomalies leaving the Arctic, and result from the export of anomalously fresh water in Davis Strait, over the east side of Belgica Bank and in the EGC, and from the import of anomalously saline water in the BSO (Figure 13). The opposite tendency is the result of fresh anomalies entering, or saline anomalies leaving, the Arctic Ocean, and they occur in the east side of Davis Strait, over the west side of Belgica Bank, through Bear Island Trough south of Bear Island and through the NCC in the BSO, and through Bering Strait. Figure 13 also shows FW fluxes by water mass, where it is seen that exports occur mainly in the Surface and Subsurface layers in Davis Strait, the EGC and over Belgica Bank, and in the AW layer in the WSC and the BSO. The most significant imports are in the Surface and Subsurface layers in eastern Davis Strait, western Belgica Bank and Bering Strait, and in saline Intermediate Water export in Fram Strait.

[56] Figure 14 shows diapycnal salinity anomaly velocity compared with diapycnal velocity, and the associated diapycnal FW and volume transports across the layer interfaces. Salinity anomaly for each layer is constrained by the model to be zero. However, as shown in Figure 8, the residual salinity anomalies (between layers 1–9) are ~0.5 Sv, equivalent to ~14 mSv FW for each layer. This suggests that the model might not properly represent the diapycnal FW distribution mechanism(s) between these layers and water masses. A large downward FW transport of ~100 mSv appears in layers 1–3. The surface FW input of 187 mSv is injected into layer 1 (see section 2.3), which was chosen as the simplest mechanism for injecting the surface FW input into the ocean in the model. However, it is clear from Figure 1 that other layers also outcrop at the surface and could also receive directly the FW input. It is possible, therefore, that the large downward FW fluxes in layers 1–3 are model artifacts: the model constraints on volume and salinity force realistic FW inputs by (effectively) taking FW from layer 1 and moving it downward, to replicate the actual inputs of FW where these layers outcrop. No significant downward FW transport below the Subsurface layer is obtained: the average salinity anomaly across layer interfaces becomes small below layer 5 (Table 2), and little diapycnal FW transport is obtained within a priori uncertainties for the calculated diapycnal salinity anomaly velocity.

[57] Figure 15 summarizes the FW budget for each water mass, where positive values show input and negative values output (export) of FW for each water mass. Shown for each water mass are (1) the net horizontal FW flux, (2) the net diapycnal flux (convergence/divergence), and (3) the model residual. For each water mass, net input plus net diapycnal flux is equal to the residual flux. The Surface water receives 187 ± 44 mSv FW input, of which 147 ± 42 mSv are exported in the ocean, 40 ± 14 mSv are exported through Fram Strait as sea ice. Also, the flux residuals in the two upper layers (Surface and Subsurface, both ~40 mSv

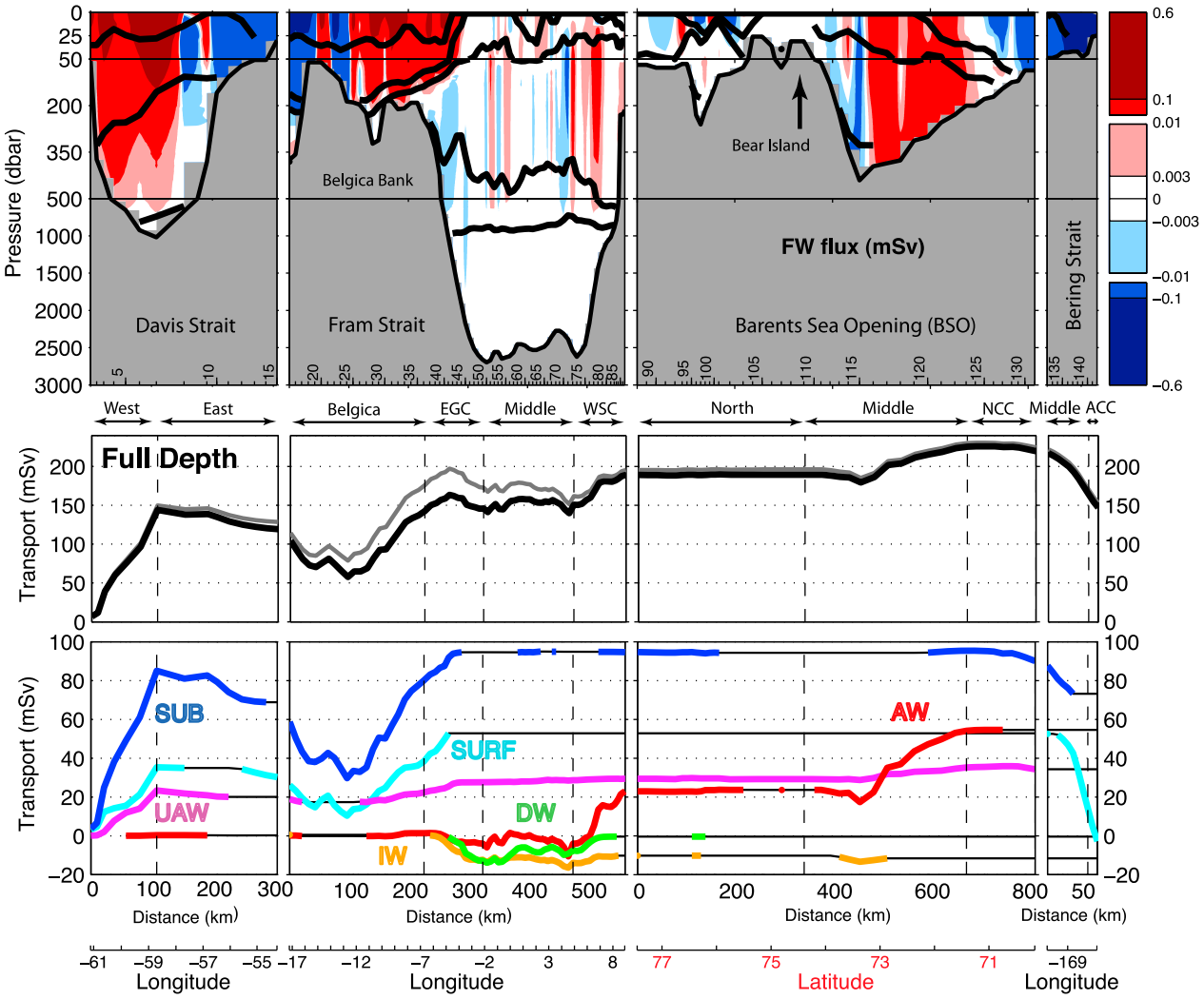

Figure 13. (top) FW flux (mSv) section calculated from the salinity and final velocity fields; bold black lines show defined water mass boundaries. (middle) Initial (gray) and final (black) accumulated full depth ocean freshwater transport (mSv) around the section, which does not include sea ice transport. (bottom) Accumulated FW flux (mSv) of the defined water masses. Where a specific water mass is absent from the section, the accumulated transport is plotted as a black line.

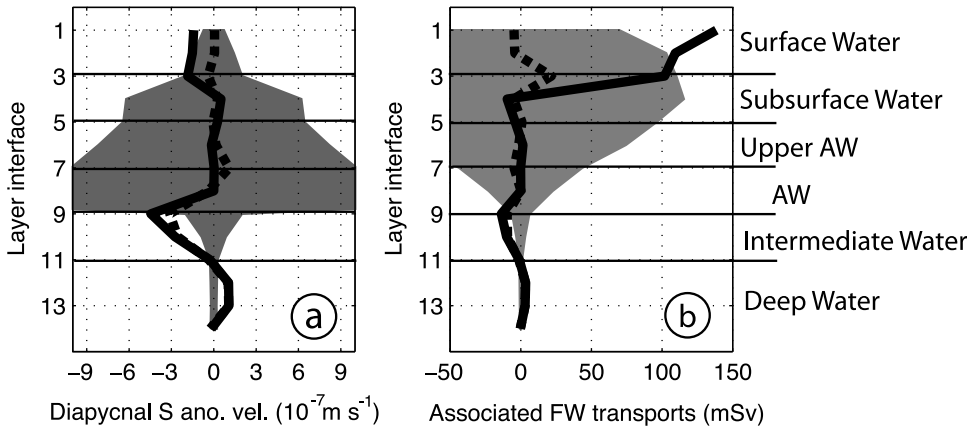

Figure 14. (a) Salinity anomaly diapycnal velocity (solid line) and volume diapycnal velocity (dotted line); positive means upward velocity. (b) Associated diapycnal FW flux (mSv) across the layer interfaces due to salinity anomaly vertical velocity (solid line) and volume vertical velocity (dotted line). The defined water mass locations are labeled. The a posteriori uncertainty is shown by gray shading.

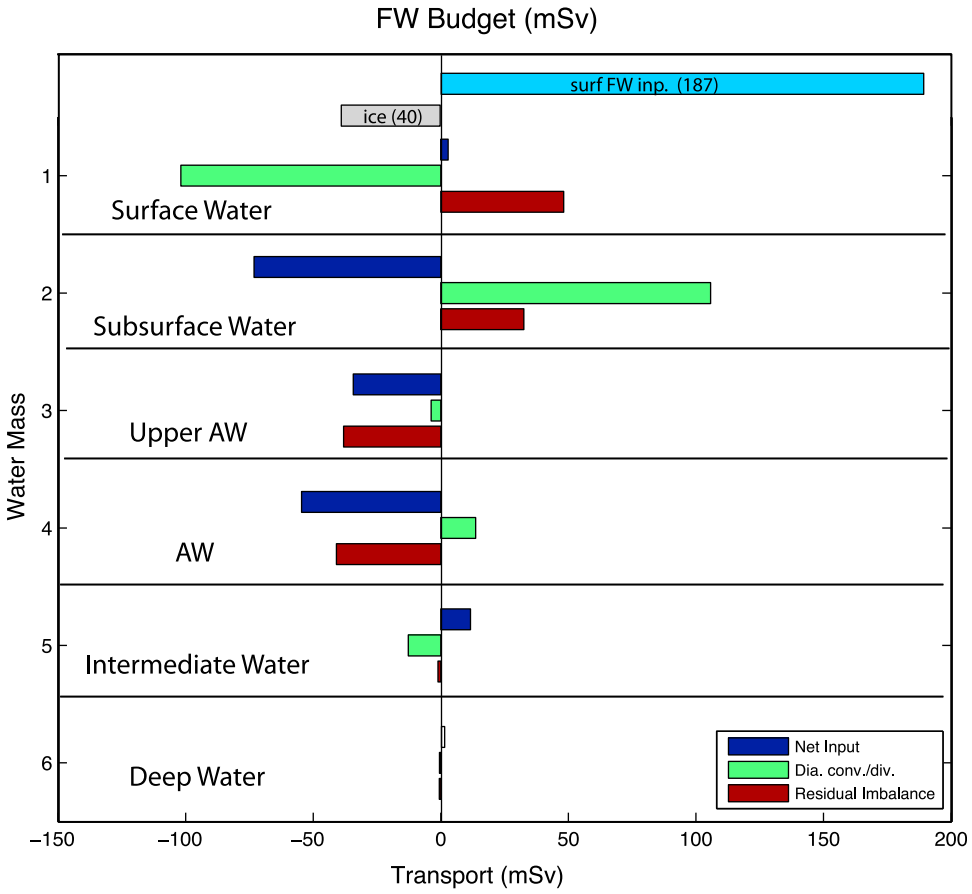

Figure 15. The FW budget (mSv) for each water mass derived from the box inverse model: net horizontal freshwater transport (dark blue), diapycnal convergence/divergence (green) and residual imbalance (dark red). The Surface layer has additional bars representing the surface FW input and sea ice flux. Positive (negative) values represent FW input (export) for each water mass. For each layer, the sum of all terms (excluding the residual) equals the residual, and the sum of all residuals equals zero.

downward) are in near-balance with the two layers immediately beneath (Upper AW and AW), which receive almost the same amount of FW (both ~40 mSv). We note above that the diapycnal salinity anomaly velocity structure may be compensation for the likely unphysical nature of the model's surface FW injection mechanism. We suggest further that the apparent balance in residual fluxes in the four uppermost layer groups may be providing more information about the nature of FW injection and mixing in the Arctic Ocean. It may be that FW is directly injected into the Upper AW layer in the Barents Sea, where sea ice is melted by contact with warm AW at the surface. The meltwater is entrained in the Barents Sea throughflow and subsequently sinks into the Arctic Ocean [*Aagaard and Woodgate*, 2001]. A second possibility is that dense waters created in winter, either in polynyas or on the wide Siberian shelves, subsequently descend and entrain upper-ocean FW on the way; this mixed product is then injected at depth into the ocean circulation [e.g., *Anderson et al.*, 1999; *Schauer et al.*, 2002b]. This quasi-direct injection of FW into layers below the surface would appear as "layer-skipping," which is not represented in the model but may be manifested by the nonzero layer flux residuals.

[58] For the net Arctic Ocean FW flux, the inversion actually makes little net difference to the initial circulation: there is some adjustment to the strength of the recirculation over Belgica Bank in Fram Strait, but otherwise the ocean FW export is 147 ± 42 mSv. Adding the Fram Strait sea ice export of 40 ± 14 mSv, the total FW export through the four main Arctic Ocean gateways, assuming stationarity, is 187 ± 44 mSv. Figure 16 shows a schematic FW budget for summer 2005.

3.4. Heat Flux

[59] With a balanced velocity field, the ocean heat flux across the Arctic Ocean boundary can be calculated. The procedure is analogous that for FW flux calculation (section 3.3), with the addition of a term for latent heat flux, noting that while Arctic Ocean imports liquid seawater, some of the export is in solid form (sea ice). Heat flux (Q) is therefore calculated as

$$Q = \oint \rho c_p v' \theta' dA + L, \tag{19}$$

where ρ is water density, c_p is seawater specific heat capacity, potential temperature (θ) anomaly $\theta' = \theta - \bar{\theta}$ and $\bar{\theta}$

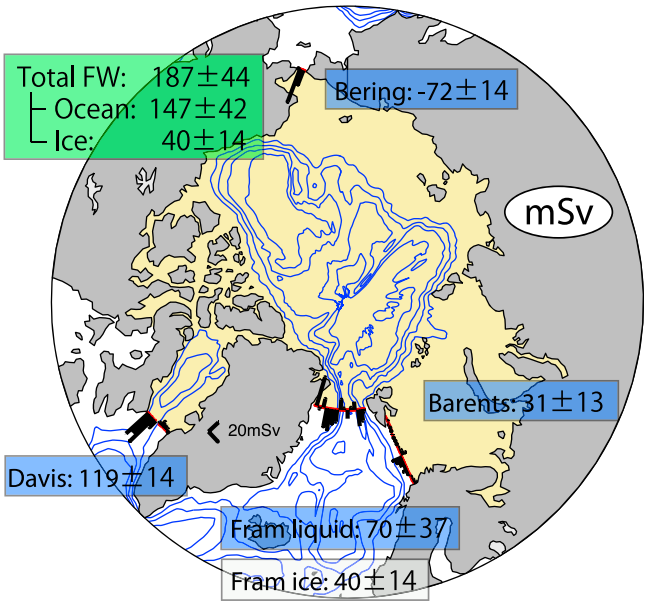

Figure 16. Schematic Arctic FW budget (mSv) in summer 2005. Total net FW transports of 187 ± 44 mSv is balanced with surface FW input, which is received in the yellow hatched area. Each component of FW sources and sinks are shown: Ocean transports are in blue boxes and Fram Strait sea ice transport in white box. Black bars along the boundary section show the ocean contribution every 40 km to the calculation of the surface FW input.

is the area-weighted mean potential temperature equal to 1.159°C, dA is a cross-section area element and L is latent heat flux due to sea ice export. Mobile sea ice is taken into account in a similar way as for the boundary mean salinity calculation. The latent heat flux is calculated using latent heat of fusion of 3.34×10^5 J kg^{-1}, giving a flux of 15 ± 5 TW. Sensible heat flux requires the ice temperature. The surface seawater temperature is −1.7°C and the average surface atmospheric temperature for August and September 2005 (78–80°N, 17–6°W) is −2 ± 1°C (obtained from the U.S. National Centers for Environmental Prediction/National Center for Atmospheric Research reanalysis project). The ice temperature is set as −1.9 ± 1.0°C, the mean of ocean and atmosphere temperatures. With a salinity of 6, the specific heat capacity is 2.98×10^4 J kg^{-1} °C^{-1} and sea ice density is 930 kg m^{-3}, and the resulting contribution to the heat flux is 4 ± 1 TW. See *Ono* [1967] for seawater heat capacities and *Timco and Frederking* [1996] for sea ice density. Figure 17 shows the heat flux (actually potential temperature anomaly transport scaled by ρc_p) section, and the accumulated heat (scaled temperature anomaly) flux around the section for full depth and for the different water masses.

[60] The total Arctic Ocean heat flux is 189 ± 26 TW, comprised of 170 ± 25 TW due to sensible (ocean) flux plus 19 ± 5 TW due to sea ice (latent and sensible heat flux). Almost half the total is carried through the BSO (86 ± 19 TW), with about a quarter entering through Fram Strait (43 ± 16 TW). The BSO dominates because it is warmer; the WSC (25 ± 5 TW) is nearer to the section-mean temperature so provides a lower contribution to the total. Substantial contributions arise from the south-going cold anomalies of Davis Strait and the EGC (28 ± 3 and 18 ± 8 TW respectively) and the north-going warm anomaly of Bering Strait (13 ± 2 TW). The AW layers dominate (69 ± 13 TW), followed by the Subsurface Water (54 ± 7 TW), Upper AW (31 ± 6 TW), and Surface Water (15 ± 1 TW).

[61] Figure 18 shows diapycnal volume and potential temperature velocity and associated diapycnal potential temperature transport. Since heat fluxes are not constrained within layers 1–11, a diapycnal potential temperature velocity profile is obtained only for layer interfaces 11–14. Therefore the diapycnal heat flux across each layer interface is estimated using the diapycnal volume flux across all layer interfaces. The diapycnal heat fluxes are estimated as the product of (area of each layer interface) × (average potential temperature on each layer interface) × (diapycnal volume velocity across the layer interface) × ρc_p. This calculation neglects other heat flux mechanisms such as diffusive diapycnal transport and Reynolds transport, and is likely to be smaller than the real vertical heat transport. Associated with the upwards volume transport of 0.8 Sv across upper AW layer, 0.8 TW heat flux has been obtained through the upper AW layers.

[62] Figure 19 summarizes the heat budget of each water mass. As shown in Figure 17, horizontal heat transport in subsurface, upper AW and AW layer brings heat into the Arctic. The total heat input to the Arctic by the ocean is 170 ± 25 TW and by sea ice is 19 ± 5 TW. Therefore the total rate of heat loss from the Arctic Ocean to the atmosphere is estimated as 189 ± 26 TW.

3.5. Sensitivity and Non-stationarity

[63] In this section, we examine the sensitivity of the inverse model results to (1) short-term oceanic variability, (2) the presence of NEMO output, (3) the representation of sea ice, (4) the exclusion from the model of a small channel in the Canadian Arctic Archipelago, and (5) the assumption of zero freshwater storage flux.

[64] First, we examine short-term oceanic variability. The inverse model adopts what is conventionally called a "quasi-stationary" data set, which means in practice that it would be hard to obtain those data in any substantially shorter time period. Even though our data fall within the same 32-day period, there can still be substantial variability within that period, whether meteorologically forced by transient weather events, or as a consequence of high-frequency oceanographic variability, such as by internal waves or inertial oscillations. In order to estimate the impact of short-term (meaning within-month) variability, we ran a modified set of models, in each of which, one of the main oceanographic features was perturbed while all others were held constant. The five features were: Bering Strait inflow, Davis Strait outflow, EGC outflow, WSC inflow and BSO inflow. The perturbation was (separately) an increase and a decrease of volume transport in each feature by 25%. All 10 perturbations changed the net FW flux by ±1–4 mSv, for a total (root-sum-square) resulting uncertainty of 6 mSv. The consequences for the net heat flux were slightly different: eight perturbations (four features) changed the net heat flux by ±1–6 TW, but the perturbations applied to one feature–the BSO–resulted in ±18 TW uncertainty. In this location, transport uncertainty feeds directly into warm

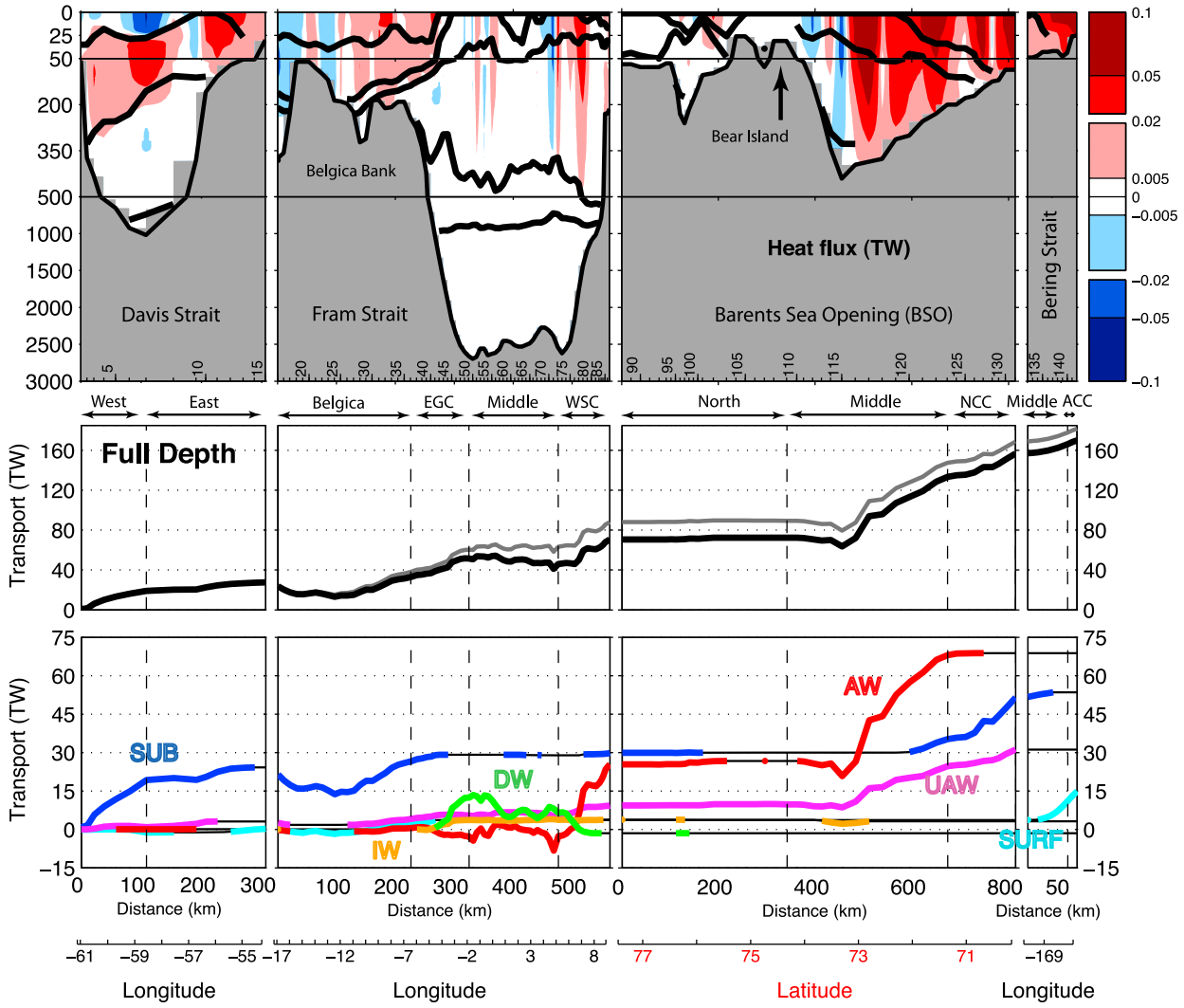

Figure 17. (top) Heat flux section calculated from the potential temperature section and final velocity field; bold black lines show defined water mass boundaries, and positive values show heat entering the Arctic. (middle) Initial (gray) and final (black) accumulated full depth heat transport around the section. (bottom) Accumulated heat flux of defined water masses; where a specific water mass is absent from the section, the accumulated transport is plotted as a black line.

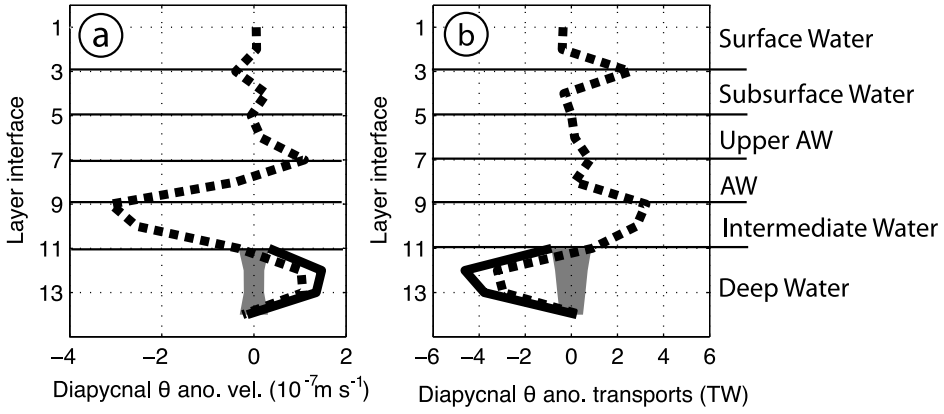

Figure 18. (a) Heat anomaly diapycnal velocity (solid line) and volume diapycnal velocity (dotted line). (b) Associated diapycnal heat transport (solid line) and volume diapycnal velocity (dotted line) across the layer interfaces. The locations of the defined water masses are labeled. The a posteriori uncertainty between interfaces 11 and 14 is shown by gray shading.

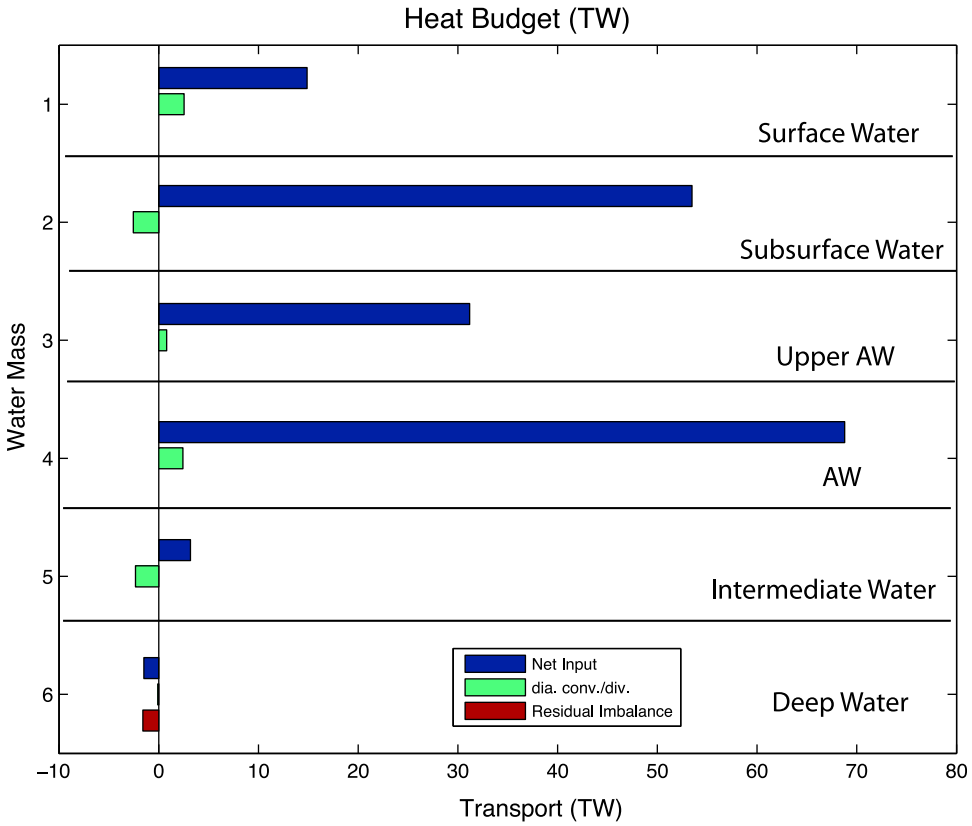

Figure 19. Heat budget for each water mass, showing net horizontal heat transport (dark blue), diapycnal convergence/divergence (green) and residual heat imbalance (dark red). Note that the calculation of convergence/divergence is based on the volume diapycnal velocity. Positive values represents heat entering a water mass. A residual is only calculated for the deepest water mass, where the inverse model requires conservation of potential temperature transport.

water transport. The total (root-sum-square) heat flux uncertainty was 20 TW.

[65] Second, we examined, in an analogous manner, the impact of the NEMO output on the inverse model solution by performing four additional inverse model runs, as follows. In run 1, there were no NEMO bottom velocities in the BSO north of Bear Island or south of 71.5°N; bottom velocities were set to zero in this region. In run 2, we eliminated all NEMO output (bottom velocities, temperature and salinity) in the BSO, so this run employs the observational data only. In run 3, we used different NEMO salinities in the Norwegian coastal region and north of Bear Island; no salinity correction was applied in the Norwegian coastal region, and 7 NEMO salinity profiles north of Bear Island were adjusted by adding a salinity of 0.2. In run 4, NEMO velocity data are replaced by VMADCP data during 1997–1999 between Bear Island and Svalbard in the BSO [*O'Dwyer et al.*, 2001]. None of the runs made a significant difference to net FW fluxes, and none of runs 1, 3, or 4 made a significant difference to net heat fluxes. Run 2, which eliminated the NEMO model output entirely, caused a significant reduction of 14 TW to net heat flux, resulting from the removal of the NCC contribution to the inverse model solution. Since run 2 is unphysical–it removes part of an oceanographic feature–it is not included in the summary uncertainty. The three remaining sensitivity runs combined produced net (additional) root-sum-square heat and FW flux uncertainties of 12 TW and 1 mSv respectively.

[66] Third, we tested the sensitivity of the standard solution to perturbations in the initial sea ice conditions. This was motivated less by the issue of short-term variability and more by uncertainty in mean sea ice thickness and advection speed. Nine sensitivity runs of the inverse model were conducted by changing the initial sea ice thickness between 1.0, 2.0 and 3.0 m, and initial sea ice advection speed between 0.10, 0.15 and 0.20 m s^{-1}, while retaining all other parameters unchanged. Initial sea ice volume fluxes ranged from 16 to 95 mSv, with a mean of 47 mSv and a standard deviation of 25 mSv. The standard deviation of final inversion solutions for (ocean and sea ice) FW flux was 17 mSv, and for surface FW input was 5 mSv. For heat flux, the standard deviations are: ocean, 4 TW; sea ice latent and sensible, 11 TW; surface, 7 TW.

[67] Fourth, we consider Fury and Hecla Strait, which lies between the Melville Peninsula of the Canadian mainland and the northwest of Baffin Island, and is the one marine exit route from the Arctic Ocean which we do not include in our inverse model. It is ~120 km long, and 15–30 km wide over much of its length, but at its eastern end where it meets Foxe Basin (to the north of Hudson Bay), through which it ultimately connects to the Atlantic Ocean via Hudson Strait and the Labrador Sea, it is effectively blocked across most of its

width by two islands, Ormonde and Eider. At this location the largest channel is ~3 km wide, and the two smaller ones <1 km. The very few measurements that have been made in the Strait are from a section ~40 km from its western end with typical depth 50 m and maximum depth 140 m. *Godin and Candela* [1987] summarize the available measurements (see references therein), and show average eastward flows between 0.03 and 0.08 Sv, based on six weeks of current meter measurements from the spring of 1972. Tides are large, ±15 cm s^{-1}, and the sub-tidal currents are directionally inconsistent, flowing both east and west (out of and into the Arctic respectively) with peak magnitudes (in both directions) similar to the tidal currents. We consider these measurements to be inadequate to resolve spatially any actual throughflow at the very narrow, partially blocked eastern end of the strait, therefore we treat them as an uncertainty. Taking a salinity of 31.5 (the observed salinity range is 31.0–32.0), using a representative transport of 0.05 Sv, and treating the circum-Arctic mean salinity as a reference value, we obtain an uncertainty due to the omission of Fury and Hecla Strait from the inverse model of 5 mSv.

[68] Fifth and finally, we examine evidence for long-term changes of FW storage in the interior of the Arctic. *McPhee et al.* [2009] and *Rabe et al.* [2011] both suggest increases of FW storage of order 8,000 km^3 over perhaps a decade, equivalent to a FW flux of 800 km^3 yr^{-1}, or $F_{stor} \sim 25$ mSv. This is a surface FW input that does not reach the ocean's exit routes and could be considered to add to the net Arctic surface FW flux. However, there is a substantial mismatch of timescales: one month for the inverse model results, a decade for the increased storage. Since we know nothing of the magnitude or even the sign of the storage term over the month in question, we can neither legitimately add the storage term to the inverse model's net FW flux, nor can we even ascribe an uncertainty.

[69] We conclude from these sensitivity tests that our model and its solution are robust, therefore, and that within the *ca.* 1 month data period, stationarity is a reasonable assumption. The root-sum-square total of the a posteriori model uncertainties (44 mSv and 26 TW; sections 3.3 and 3.4) with the preceding values in this section for the uncertainties due to short-term variability, NEMO, sea ice, and Fury and Hecla Strait are 48 mSv and 37 TW.

4. Discussion and Conclusions

4.1. "Reference" Values

[70] The use of arbitrary "reference" values as part of attempts to calculate heat and FW fluxes is widespread in the literature. A referenced calculation of FW flux looks like this

$$F^* = \frac{\oint S^* v' dA}{S_{ref}}, \tag{20}$$

where $S^* = S - S_{ref}$ and S_{ref} is the assumed reference salinity. The same arguments apply to heat flux calculations using reference temperatures. "Referenced" quantities are denoted by the asterisk. F^* is related to F (see Appendix A) by

$$F^* = \left(\frac{\bar{S}}{S_{ref}}\right) F \tag{21}$$

so for any sensible choice of S_{ref}, the estimation of total net surface flux given an enclosed area of ocean may be in error by (typically) 1–2%; this size of error is not noticeable given other, much larger, sources of uncertainty. The integral in (20) is little affected by error in the reference salinity because the integral expresses the net transport of a property where there exists directional correlation, meaning (for example) north-going positive salinity anomalies and south-going negative salinity anomalies. If the reference salinity is wrong, then the integral calculation exactly balances an overestimate in one direction by an underestimate in the other direction when taken around the entire boundary (see Appendix A)

$$\oint S^* v' dA = \oint S' v' dA. \tag{22}$$

Therefore the error in the resulting *net* flux is solely due to the error in S_{ref} in the denominator of (20).

[71] However, the fact that F^* may be only slightly in error masks a much greater potential for error in the use of reference values. While net flux calculations are quite insensitive to (sensible) choices of S_{ref}, the individual flux components are highly sensitive. Imagine making a partial calculation, say of the EGC only, using (20), which we expand, and noting that the integral is no longer around the complete circuit

$$\begin{aligned} F^* &= \frac{\int S^* v' dA}{S_{ref}} \\ &= \frac{\int (\bar{S} - S_{ref} + S') v' dA}{S_{ref}} \\ &= \frac{\delta S \int v' dA}{S_{ref}} + \frac{\bar{S}}{S_{ref}} \cdot F, \end{aligned} \tag{23}$$

where δS is the difference between the circum-Arctic mean salinity $\bar{S}$ and the reference salinity S_{ref}. The second term on the RHS is almost the same as the correct calculation (cf. (21) above), but the first term biases the calculation by a quantity dependent on the current's volume transport ($\int v' dA$) and δS, the difference between the circum-Arctic mean salinity $\bar{S}$ and the reference salinity S_{ref}. For the EGC transport of ~5 Sv, and with $\delta S = 0.2$ and $S_{ref} = 34.8$, the resulting error in the FW flux calculation is ~30 mSv. This effect of arbitrary choices of reference values of temperature and salinity for heat and FW calculation is illustrated in Figure 20, in which the circum-Arctic integration of heat and FW fluxes is repeated, and set beside referenced calculations using a reference temperature of −0.1°C and reference salinities of 34.8 and 35.0. This clearly demonstrates both points: (1) net fluxes for an enclosed region are barely affected by use of reference values but (2) the component transports are substantially affected.

[72] Many scientists are accustomed to the use of reference salinities in the estimation of FW fluxes, and it is an established habit to consider the volume-mean salinity (for the Arctic in this case) as the appropriate reference. We have shown the potential for error in this approach, and we

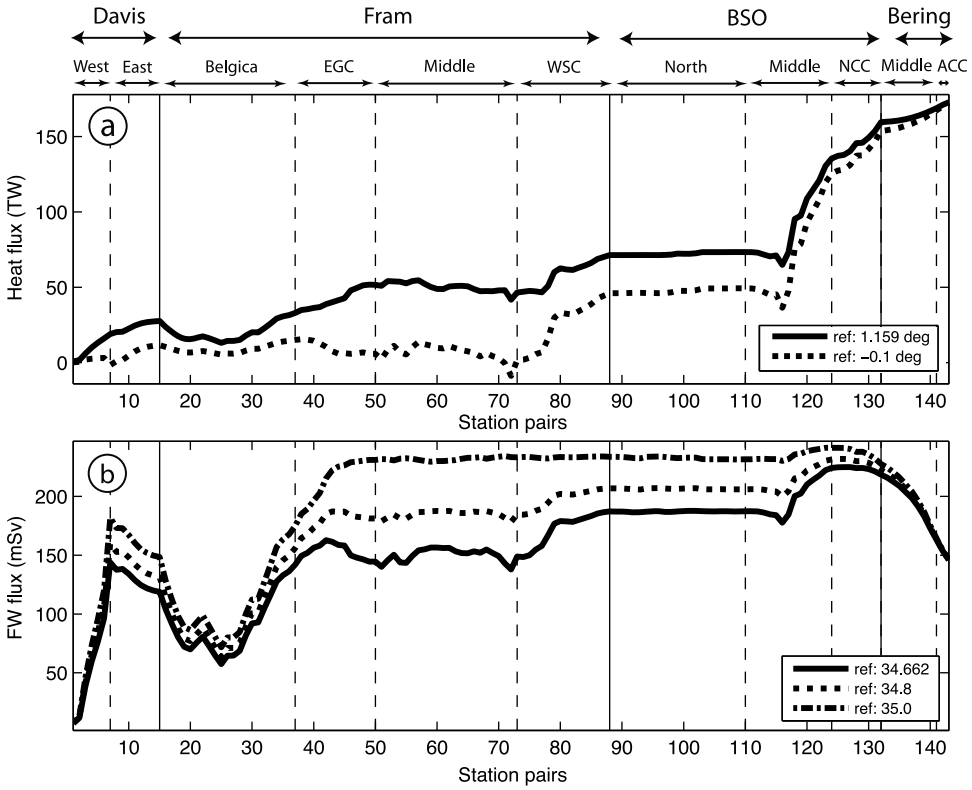

Figure 20. Illustration of the consequences of use of arbitrary reference values: (a) accumulated heat flux around the section comparing the model solution (solid line; mean potential temperature 1.159°C) with use of a reference potential temperature of −0.1°C (dotted line) and (b) accumulated freshwater flux comparing the inverse model solution (solid line; mean salinity 34.662) with use of reference salinities of 34.8 (dotted line) and 35.0 (dash-dotted line). Vertical solid lines shows the boundaries of each strait, and vertical dashed lines show the sub-divisions of each Strait.

attempt further clarification. Consider again the volume of the Arctic Ocean, enclosed by boundaries, which are the sides, comprised of land and ocean, and the surface. The *status quo* for salinity within the volume is maintained solely by the side (ocean) salinity transport. As long as the import salinity flux is the same as the export salinity flux, it does not matter to the present internal volume-mean salinity how the balance of boundary fluxes is achieved. It can be via large or small volume fluxes, or via large or small salinity anomalies. The boundary-mean salinity has no necessary connection with the interior mean salinity.

[73] Prompted by consideration of the interior, volume-mean salinity of the Arctic, we note further that it seems not to be the often-quoted value of 34.8. *Aagaard and Carmack* [1989] estimated the volume mean salinity of the Arctic as 34.80 ± 0.04 based on the World Ocean Atlas 1983 [*Gorshkov*, 1983] and other data sources. The calculation appears not to have included sea ice. We recalculated the volume mean salinity of the Arctic enclosed by the four main gateways (Davis, Fram and Bering Straits, and the BSO) using the PHC data set [*Steele et al.*, 2001] and a sea ice volume estimate [*Zhang and Rothrock*, 2003]. The calculated annual volume-mean salinity in the Arctic including sea ice is 34.69. The summer (July–September) and winter (March–May) values are 34.69 and 34.68 respectively. They are derived from ocean-only means of 34.72 (summer) and 34.74 (winter) combined with sea ice volumes of 13×10^{12} and 28×10^{12} m^3 respectively, and using a sea ice salinity of 6. This value (34.69) turns out to be somewhat closer to our boundary mean salinity of 34.66 than the conventional Arctic volume-mean salinity of 34.8. We note in passing that increased FW storage of 8000 km^3 (section 3.5) is equivalent to a reduction in mean Arctic Ocean salinity of 0.02. Identification of the causes of the difference in mean salinities merits further study, but it is beyond the scope of this work to pursue it further.

4.2. Comparisons With Previous Studies

[74] As far as the authors are aware, of the many other previous studies that calculate component heat and FW fluxes, none uses reference values close to the circum-Arctic mean, as is done here; and it is beyond the scope of the present study to attempt to re-calculate those fluxes (after equation (23) and the following). However, we can take recent examples of such calculations–in the same locations as used in the present study–and compare them with the present fluxes recalculated using the other authors' reference values, as a check on consistency.

[75] Davis and Bering Strait FW fluxes (132 mSv and 76 mSv respectively) referenced to 34.8 agree with recent studies. *Curry et al.* [2011] estimate 116 ± 41 mSv FW outflow in Davis Strait based on 2004–2005 mooring

observations referenced to 34.8. *Woodgate and Aagaard* [2005] estimate 80 ± 10 mSv FW inflow in Bering Strait referenced to 34.8 based on 1991–2004 mooring observations.

[76] In Fram Strait, the FW flux over Belgica Bank is still poorly known due to the lack of direct velocity observations [*Rabe et al.*, 2009; *de Steur et al.*, 2009]. *De Steur et al.* [2009] estimate the annual mean liquid FW outflow in the EGC region (6.5–0.0°W), referenced to 34.9, as 40.4 ± 14.4 mSv based on 1998–2008 mooring observations. This value is similar to our liquid FW flux of 44 mSv, for the same region and reference salinity. *Rabe et al.* [2009] estimate a liquid FW outflow of 80 mSv referenced to 34.92 from the eastern edge of the Belgica Bank recirculation (10.6°W) to 4°E based on 2005 summer CTD, mooring and VMADCP data. When we recalculate the FW flux with the inverted velocity field over the same zonal range and with the same reference salinity, the FW flux is similar: 73 mSv.

[77] The BSO FW flux referenced to 35.0 (using our sign convention) is −6 mSv, compared to −17 mSv by *Smedsrud et al.* [2010], who use mooring observations and a reference salinity of 35.0. Their estimate comprises −22.7 mSv in the NCC and 5.7 mSv due to AW in the central BSO. Our −6 mSv estimate is obtained from −14 mSv in the NCC, 12 mSv due to AW in the central BSO, −2 mSv south of Bear Island and −2 mSv between Bear Island and Svalbard. The difference between the two estimates mainly arises from the different volume transport estimates for the NCC: theirs is 1.2 Sv, ours is 0.8 ± 0.4 Sv.

[78] The BSO heat flux is 103 TW referenced to 0.0°C, which is larger than the estimate of 73 TW referenced to 0.0° C [*Smedsrud et al.*, 2010]. This is mainly due to the AW volume inflow in the central BSO being larger by 1.5 Sv. Based on the volume transport sensitivity test of *Smedsrud et al.* [2010], their 73 TW heat transport becomes 108 TW if AW volume transport increases by 1.5 Sv. Davis Strait heat transport referenced to −0.1°C is 11 TW. This is comparable to the latest annual mean heat transport estimate of 20 ± 9 TW [*Curry et al.*, 2011]. Bering Strait heat transport referenced to −1.9°C is 26 TW. This agrees well with the latest heat flux estimate of about 23 TW, which includes a correction of 3 TW for the Alaskan Coastal Current, during August and October 2005, referenced to −1.9°C [*Woodgate et al.*, 2010, Figure 3]. WSC heat flux referenced to −0.1°C is 44 TW. This is again comparable to the recent annual mean heat transport estimate of 28–44 TW referenced to −0.1°C based on mooring observations during 1997–2000 [*Schauer et al.*, 2004]. *Schauer et al.* [2008] and *Schauer and Beszczynska-Möller* [2009] estimate decadal WSC heat transports since 1998 employing the newly defined "tube" method. The heat transport with arbitrary reference temperature during 2003–2007 is 40–50 TW. When we calculate heat transport with an arbitrary reference temperature, from the eastern boundary of Fram Strait to 5.2°W, where WSC inflow is balanced with outflow, the heat transport in this section is 35 TW. This relatively small heat transport compares well with the Fram Strait heat flux for mid-2005 shown by *Schauer et al.* [2008, Figure 3.10].

[79] The diapycnal potential temperature anomaly transport across the upper AW layer referenced to 0.0°C is 4.6 (TW). This is equivalent to about 0.6 W m^{-2} across the entire Arctic Ocean interior. This agrees with a local direct microstructure estimation of diffusive heat flux of 1.0 W m^{-2} offshore of the Laptev Sea [*Lenn et al.*, 2009].

4.3. Net Heat and Freshwater Fluxes

[80] The only existing inverse model study to include Arctic Ocean and sea ice circulation and fluxes is that of *Mauritzen* [1996a, 1996b], who employs an asynoptic collection of hydrographic data from the summers of 1980–1989. Her model uses separate boxes for the Barents Sea and the rest of the Arctic Ocean, and by summing her solution's surface heat fluxes for these areas, we find that her net heat flux is 96 TW (±20%), which is half the size of ours, at 189 ± 37 TW. There is no explicit FW flux calculation. We can attempt to identify reasons for the different heat fluxes.

[81] First, as noted at the end of section 4.2, our stronger BSO fluxes can account for ∼35 TW of the difference. Second, *Holliday et al.* [2008] show multidecadal time series of (among other properties) WSC and BSO temperatures, which have substantially increased between the 1980s and 2005. *Holliday et al.* [2008] represent the WSC by the Fram Strait and Sørkapp hydrographic sections, and by the BSO by the Fugløya-Bear Island sections, respectively (their Figures 1 and 2). We can conduct some simple numerical experiments with our inverse model in line with *Holliday et al.* [2008] by altering upper-ocean temperatures because they are not conservative variables in the model. Reducing AW temperatures by 1 or 2°C either in the upper 200 m or the upper 500 m reduces the net heat flux by 18–53 TW. The different depth ranges result from the specifications of *Holliday et al.* [2008]. The different temperatures depend on how data from the 1980s are employed. Therefore between half and most of the net heat flux difference between *Mauritzen* [1996a, 1996b] and the present study results from (1) our stronger BSO inflow and (2) the higher AW temperatures prevalent in the last decade or so. Any remaining difference is likely due to model formulation, data availability and/or data characteristics in the earlier study.

[82] Our heat flux represents a net heat loss by the ocean to the atmosphere of 189 ± 37 TW. Scaled by the ocean surface area (section 2.1), this is equivalent to 16.7 ± 3.3 W m^{-2}. It is hard to reconcile this result with the ocean heat flux calculations of *Serreze et al.* [2006, Table 2]. It is not close to his peak monthly summer or winter values of *ca.* 1,000 TW input to the ocean or 500 TW loss from the ocean (respectively). It most nearly resembles his annual mean value of 11 W m^{-2}, equivalent to 105 TW loss from the ocean. Perhaps it should not be surprising that there is no simple coincidence between our heat flux results, however, given (1) the very different methodologies and (2) the long residence times of water masses within the Arctic Ocean, which will (to some extent) smooth out monthly to interannual (maybe even decadal) variations in the ocean result.

[83] Our total net FW transport is 187 ± 48 mSv, equivalent to 5,930 ± 1,510 km^3 yr^{-1}; scaled by surface area, this is equivalent to (1.65 ± 0.42) × 10^{-8} m s^{-1}, or 1.43 ± 0.37 mm day^{-1}. It does not include the long-term FW storage term of ∼25 mSv. This is similar to the 149–237 mSv estimate of *Dickson et al.* [2007] but somewhat smaller than the value of *Serreze et al.* [2006]. We note that the ocean data are all (largely) obtained in the summer.

[84] The present results are summarized in Figure 21, which is a net volumetric θ-S plot. The entire circum-Arctic

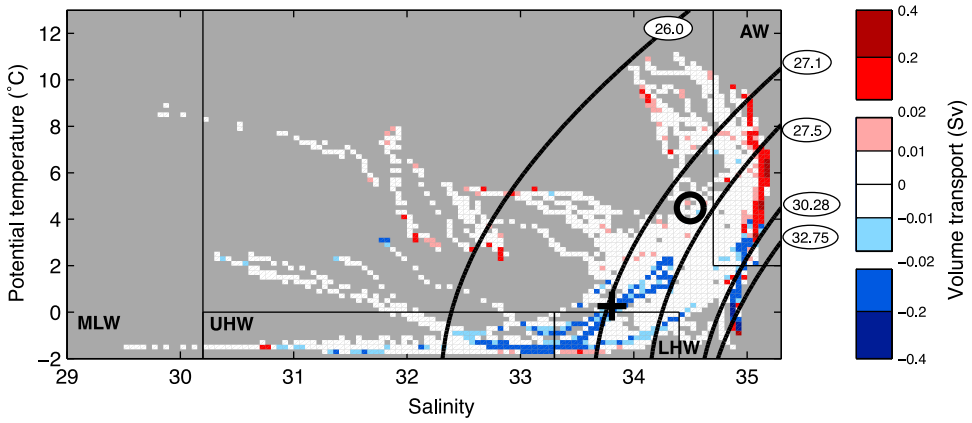

Figure 21. Volumetric θ-S plot gridded with $\delta\theta$ = 0.2°C and δS = 0.05. Model water mass boundaries (densities) are shown in black. These corresponding densities are 26.0 σ_0, 27.1 σ_0, 27.5 σ_0, 30.28 $\sigma_{0.5}$, and 32.75 $\sigma_{1.0}$. Net transport per θ-S grid box is shaded with red for inflow and blue for outflow (Sv). Grey shading indicates no data. The transport-weighted mean properties of the inflow (bold circle) are: salinity 34.50, potential temperature 4.49°C, density (σ_0) 27.34 kg m^{-3}; for the outflow (bold cross), including sea ice, they are 33.81, 0.25°C, and 27.13 kg m^{-3}. Some conventional water masses in the central Arctic (MLW, UHW, LHW, and AW) are shown based on *Aksenov et al.* [2010, Table 2].

section is projected onto the θ-S plane, which is gridded with $\delta\theta$ = 0.2°C and δS = 0.05. All transports within each θ-S grid box are summed and the net transport in that class is plotted. Imports are colored red and exports colored blue. Only the remaining net fluxes appear, so that (for example) an eddy carrying identical water into and out of the section will vanish. The transport-weighted mean (net) inflow is at 4.49°C, salinity 34.50 and potential density σ_0 = 27.34 kg m^{-3}. The corresponding values for the outflow (including sea ice) are 0.25°C, salinity 33.81 and potential density σ_0 = 27.13 kg m^{-3}, respectively. The net effect of the Arctic is to freshen and cool the inflows by 0.69 in salinity and 4.23°C, and (in summer), there is a net input of buoyancy shown by the decrease in mean density of 0.21 kg m^{-3}.

[85] Finally, while the inverse method is clear and our input data are as complete and as synoptic as possible, it is not clear to what degree the present results may (or may not be) representative of other summers or of annual mean fluxes. The immediate question arising from this work concerns the magnitude of the annual cycle of Arctic Ocean heat and freshwater fluxes, which we plan to address in a future study.

Appendix A: Reference Salinities

[86] Consider what happens to the calculation of surface FW flux F if an arbitrary reference salinity, S_{ref}, is used instead of the boundary-mean salinity $\bar{S}$. Denote quantities calculated using S_{ref} with the asterisk

$$F^* = \frac{\oint S^* v' \, dA}{S_{ref}}, \tag{A1}$$

where

$$\begin{aligned} S^* &= S - S_{ref} \\ &= \bar{S} + S' - S_{ref}. \end{aligned} \tag{A2}$$

By construction of v', addition or removal of constant values to S within integrals makes identically zero contribution to the calculation of either F or F*, so

$$\oint S' v' \, dA = \oint S^* v' \, dA. \tag{A3}$$

The difference between (7) and (A1) lies in the denominator: the quantity by which the integral is "scaled" to calculate the FW flux F. The calculation of F* is therefore formally incorrect because it violates mass conservation. Consider the salinity transport T_S which is the area integral of the product of salinity and velocity

$$\begin{aligned} T_S &= \oint S v \, dA \\ &= \oint \left(S_{ref} + S^*\right)(\bar{v} + v') \, dA \\ &= \bar{v} A S_{ref} + \bar{v} \oint S^* \, dA + S_{ref} \oint v' \, dA + \oint v' S^* \, dA \end{aligned} \tag{A4}$$

Set T_S equal to zero (conservation of salinity transport), rearrange and divide throughout by S_{ref}

$$-\bar{v} A = \frac{\bar{v} \oint S^* \, dA}{S_{ref}} + \oint v' \, dA + \frac{\oint v' S^* \, dA}{S_{ref}}. \tag{A5}$$

Now examine each term in (A5). The left-hand side is the net ocean volume flux, equal to the FW flux

$$-\bar{v} A = -V_0 = F. \tag{A6}$$

The first term on the right-hand side (RHS) of (A5) is the "missing" component of the net FW flux due to use of an assumed reference salinity instead of the correct mean

$$\frac{\bar{v} \oint S^* \, dA}{S_{ref}} = \frac{\bar{v} \oint \left(S' + \bar{S} - S_{ref}\right) \, dA}{S_{ref}} = -F \frac{\left(\bar{S} - S_{ref}\right)}{S_{ref}}. \tag{A7}$$

The second term on the RHS of (A5) is equal to zero by construction of the anomalies. The third term on the RHS of (A5) is a scaled FW flux and is equal to F^*

$$\frac{\oint v'S^* dA}{S_{ref}} = \frac{\oint v'S' dA}{S_{ref}} = F\left(\frac{\bar{S}}{S_{ref}}\right) = F^*. \qquad \text{(A8)}$$

The sum of (A7) and (A8), the two nonzero terms on the RHS of (A5), is F. These last two equations express how the use of an assumed reference salinity violates conservation of mass; (A8) is the "usual" calculation, which will be in error in a sense dependent on choice of S_{ref}; and (A7) is the amount by which (A8) is in error due to this assumption.

[87] **Acknowledgments.** This study was funded by the UK Natural Environment Research Council as a contribution to the Arctic IPY project ASBO. ACNG's involvement was partially supported by a NERC Advanced Research Fellowship (NE/C517633/1) and a Philip Leverhulme Prize. The Bering Strait data were collected by the University of Washington, Seattle, USA and the University of Alaska, Fairbanks, USA (PIs Woodgate and Weingartner) with funding from ONR, NSF, and NOAA. The data are freely available via http://psc.apl.washington.edu/BeringStrait.html and the National Ocean Data Center (USA). The whole Bering Strait CTD section was collected under the protocol of the Russian-American Long-term Census of the Arctic (RUSALCA; http://www.arctic.noaa.gov/aro/russian-american/). Mrs. Beverly de Cuevas (National Oceanography Centre Southampton) provided this study with the NEMO GCM output. The 1/4° NEMO run (ORCA025-N206) was undertaken as part of the DRAKKAR collaboration [*Barnier et al.*, 2006]. NCEP/NCAR reanalysis output was obtained from the Web site of NOAA/ESRL Physical Sciences Division, Boulder, Colorado, at http://www.esrl.noaa.gov/psd/. Two anonymous revewers comments helped to improve the manuscript.

References

Aagaard, K., and E. Carmack (1989), The role of sea ice and other fresh-water in the Arctic circulation, *J. Geophys. Res.*, *94*(C10), 14,485–14,498, doi:10.1029/JC094iC10p14485.

Aagaard, K., and R. A. Woodgate (2001), Some thoughts on the freezing and melting of sea ice and their effects on the ocean, *Ocean Modell.*, *3*, 127–135, doi:10.1016/S1463-5003(01)00005-1.

Agnew, T., A. Lambe, and D. Long (2008), Estimating sea ice area flux across the Canadian Arctic Archipelago using enhanced AMSR-E, *J. Geophys. Res.*, *113*, C10011, doi:10.1029/2007JC004582.

Aksenov, Y., S. Bacon, A. C. Coward, and N. P. Holliday (2010), Polar outflow from the Arctic Ocean: A high resolution model study, *J. Mar. Syst.*, *83*, 14–37, doi:10.1016/j.jmarsys.2010.06.007.

Anderson, L. G., E. P. Jones, and B. Rudels (1999), Ventilation of the Arctic Ocean estimated by a plume entrainment model constrained by CFCs, *J. Geophys. Res.*, *104*(C6), 13,423–13,429, doi:10.1029/1999JC900074.

Barnier, B., et al. (2006), Impact of partial steps and momentum advection schemes in a global ocean circulation model at eddy-permitting resolution, *Ocean Dyn.*, *56*(5–6), 543–567, doi:10.1007/s10236-006-0082-1.

Blindheim, J. (1989), Cascading of Barents Sea bottom water into the Norwegian Sea, *Rapp. P.-V. Reun. – Cons. Int. Explor. Mer*, *188*, 49–58.

Boyer, T. P., et al. (2009), *World Ocean Database 2009*, vol. 1, *Introduction, NOAA Atlas NESDIS*, vol. 66, edited by S. Levitus, 216 pp., NOAA, Silver Spring, Md.

Carmack, E. C. (2000), The Arctic Ocean's freshwater budget: Sources, storage and export, in *The Freshwater Budget of the Arctic Ocean*, edited by E. L. Lewis et al., pp. 91–126, Kluwer Acad., Dordrecht, Netherlands.

Carmack, E. C., K. Aagaard, J. H. Swift, R. W. Macdonald, F. A. Mclaughlin, E. P. Jones, R. G. Perkin, J. N. Smith, K. M. Ellis, and L. R. Killius (1997), Changes in temperature and tracer distributions within the Arctic Ocean: Results from the 1994 Arctic Ocean section, *Deep Sea Res., Part II*, *44*, 1487–1502, doi:10.1016/S0967-0645(97)00056-8.

Cuny, J., P. B. Rhines, and R. Kwok (2005), Davis Strait volume, freshwater and heat fluxes, *Deep Sea Res., Part I*, *52*(3), 519–542, doi:10.1016/j.dsr.2004.10.006.

Curry, B., C. M. Lee, and B. Petrie (2011), Volume, freshwater, and heat fluxes through Davis Strait, 2004–05, *J. Phys. Oceanogr.*, *41*(3), 429–436, doi:10.1175/2010JPO4536.1.

Curry, R. (2001), HydroBase 2—A database of hydrographic profiles and tools for climatological analysis, technical reference, 81 pp., Natl. Sci. Found., Arlington, Va. [Available at http://www.whoi.edu/science/PO/hydrobase/.]

de Steur, L., E. Hansen, R. Gerdes, M. Karcher, E. Fahrbach, and J. Holfort (2009), Freshwater fluxes in the East Greenland Current: A decade of observations, *Geophys. Res. Lett.*, *36*, L23611, doi:10.1029/2009GL041278.

Dickson, R., B. Rudels, S. Dye, M. Karcher, J. Meincke, and I. Yashayaev (2007), Current estimates of freshwater flux through Arctic and subarctic seas, *Prog. Oceanogr.*, *73*(3–4), 210–230, doi:10.1016/j.pocean.2006.12.003.

Fahrbach, E., and P. Lemke (2005), The expedition ARKTIS-XXI/1 a and b of the Research Vessel "Polarstern" in 2005, in *ARK-XX/2 Cruise Report*, edited by G. Budeus, E. Fahrbach, and P. Lemke, pp. 57–142, Alfred-Wegener-Inst., Bremerhaven, Germany.

Fahrbach, E., J. Meincke, S. Osterhus, G. Rohardt, U. Schauer, V. Tverberg, and J. Verduin (2001), Direct measurements of volume transports through Fram Strait, *Polar Res.*, *20*(2), 217–224, doi:10.1111/j.1751-8369.2001.tb00059.x.

Fer, I., R. Skogseth, P. M. Haugan, and P. Jaccard (2003), Observations of the Storfjorden overflow, *Deep Sea Res., Part I*, *50*(10–11), 1283–1303, doi:10.1016/S0967-0637(03)00124-9.

Furevik, T. (2001), Annual and interannual variability of Atlantic Water temperatures in the Norwegian and Barents Seas: 1980–1996, *Deep Sea Res., Part I*, *48*(2), 383–404, doi:10.1016/S0967-0637(00)00050-9.

Ganachaud, A. (1999), Large scale oceanic circulation and fluxes of freshwater, heat, nutrients and oxygen, PhD thesis, 267 pp., Mass. Inst. of Technol./Woods Hole Oceanogr. Inst. Jt. Program, Cambridge, Mass.

Ganachaud, A., and C. Wunsch (2000), Improved estimates of global ocean circulation, heat transport and mixing from hydrographic data, *Nature*, *408*, 453–457, doi:10.1038/35044048.

Gill, A. E. (1983), *Atmosphere-Ocean Dynamics*, 662 pp., Academic, London.

Godin, G., and J. Candela (1987), Tides and currents in Fury and Hecla Strait, *Estuarine Coastal Shelf Sci.*, *24*, 513–525, doi:10.1016/0272-7714(87)90131-4.

Golubev, A., C. Zuyev, and C. Oelke (2000), BarKode: The Barents and Kara Seas oceanographic data base (1898–1998), report, Norw. Polar Inst., Tromsø, Norway. [Available at http://acsys.npolar.no/adis/datasets/barkode/barkode.php.]

Gorshkov, S. G. (1983), *World Ocean Atlas: Arctic Ocean* (in Russian), vol. 3, 189 pp., Pergamon, New York.

Grist, J. P., S. A. Josey, R. Marsh, S. A. Good, A. C. Coward, B. A. de Cuevas, S. G. Alderson, A. L. New, and G. Madec (2010), The roles of surface heat flux and ocean heat transport convergence in determining Atlantic Ocean temperature variability, *Ocean Dyn.*, *60*, 771–790, doi:10.1007/s10236-010-0292-4.

Holliday, N. P., et al. (2008), Reversal of the 1960s to 1990s freshening trend in the northeast North Atlantic and Nordic Seas, *Geophys. Res. Lett.*, *35*, L03614, doi:10.1029/2007GL032675.

Ingvaldsen, R., H. Loeng, and L. Asplin (2002), Variability in the Atlantic inflow to the Barents Sea based on a one-year time series from moored current meters, *Cont. Shelf Res.*, *22*(3), 505–519, doi:10.1016/S0278-4343(01)00070-X.

Ingvaldsen, R., L. Asplin, and H. Loeng (2004), The seasonal cycle in the Atlantic transport to the Barents Sea during the years 1997–2001, *Cont. Shelf Res.*, *24*, 1015–1032, doi:10.1016/j.csr.2004.02.011.

Intergovernmental Panel on Climate Change (2007), *Climate Change 2007: The Physical Science Basis: Working Group I Contribution to the Fourth Assessment Report of the Intergovernmental Panel on Climate Change*, edited by S. Solomon et al., 996 pp., Cambridge Univ. Press, New York.

Jakobsson, M. (2002), Hypsometry and volume of the Arctic Ocean and its constituent seas, *Geochem. Geophys. Geosyst.*, *3*(5), 1028, doi:10.1029/2001GC000302.

Kwok, R. (2004), Fram Strait sea ice outflow, *J. Geophys. Res.*, *109*, C01009, doi:10.1029/2003JC001785.

Kwok, R. (2006), Exchange of sea ice between the Arctic Ocean and the Canadian Arctic Archipelago, *Geophys. Res. Lett.*, *33*, L16501, doi:10.1029/2006GL027094.

Kwok, R. (2007), Near zero replenishment of the Arctic multiyear sea ice cover at the end of 2005 summer, *Geophys. Res. Lett.*, *34*, L05501, doi:10.1029/2006GL028737.

Lee, C. M., J. Abriel, J. I. Gabat, B. Petrie, M. Scotney, V. Soukhovtsev, and K. V. Thiel (2004), An observational array for high-resolution, year-round measurements of volume, freshwater, and ice flux variability in Davis Strait: Cruise report for R/V *Knorr* 179–05, 22 September–4 October 2004, report, Univ. of Wash., Seattle, Wash. [Available at http://iop.apl.washington.edu/projects/ds/html/publications.php/APL_UW_TR_0408.pdf.]

Lenn, Y. D., et al. (2009), Vertical mixing at intermediate depths in the Arctic boundary current, *Geophys. Res. Lett.*, *36*, L05601, doi:10.1029/2008GL036792.

Lique, C., A. M. Treguier, M. Scheinert, and T. Penduff (2009), A model-based study of ice and freshwater transport variability along both sides of Greenland, *Clim. Dyn.*, *33*(5), 685–705, doi:10.1007/s00382-008-0510-7.

Lique, C., A. M. Treguier, B. Blanke, and N. Grima (2010), On the origins of water masses exported along both sides of Greenland: A Lagrangian model analysis, *J. Geophys. Res.*, *115*, C05019, doi:10.1029/2009JC005316.

Loeng, H. (1991), Features of the physical oceanographic conditions of the Barents Sea, *Polar Res.*, *10*(1), 5–18, doi:10.1111/j.1751-8369.1991.tb00630.x.

Marsh, R., D. Desbruyères, J. L. Bamber, B. A. de Cuevas, A. C. Coward, and Y. Aksenov (2010), Short-term impacts of enhanced Greenland freshwater fluxes in an eddy-permitting ocean model, *Ocean Sci.*, *6*, 749–760, doi:10.5194/os-6-749-2010.

Mauritzen, C. (1996a), Production of dense overflow waters feeding the North Atlantic across the Greenland-Scotland Ridge. Part 1: Evidence for a revised circulation scheme, *Deep Sea Res., Part I*, *43*(6), 769–806, doi:10.1016/0967-0637(96)00037-4.

Mauritzen, C. (1996b), Production of dense overflow waters feeding the North Atlantic across the Greenland-Scotland Ridge. Part 2: An inverse model, *Deep Sea Res., Part I*, *43*(6), 807–835, doi:10.1016/0967-0637(96)00038-6.

McIntosh, P. C., and S. R. Rintoul (1997), Do box inverse models work?, *J. Phys. Oceanogr.*, *27*(2), 291–308, doi:10.1175/1520-0485(1997)027<0291:DBIMW>2.0.CO;2.

McPhee, M. G., A. Proshutinsky, J. H. Morison, M. Steele, and M. B. Alkire (2009), Rapid change in freshwater content of the Arctic Ocean, *Geophys. Res. Lett.*, *36*, L10602, doi:10.1029/2009GL037525.

Melling, H., T. A. Agnew, K. K. Falkner, D. A. Greenberg, C. M. Lee, A. Munchow, B. Petrie, R. M. Prinssenberg, R. M. Samelson, and R. A. Woodgate (2008), Fresh-water fluxes via Pacific and Arctic outflows across the Canadian Polar Shelf, in *Arctic-Subarctic Ocean Fluxes: Defining the Role of the Northern Seas in Climate*, edited by R. R. Dickson, J. Meincke, and P. Rhines, pp. 193–247, Springer, Dordrecht, Netherlands.

Mernild, S. H., G. E. Liston, C. A. Hiemstra, K. Steffen, E. Hanna, and J. H. Christensen (2009), Greenland Ice Sheet surface mass-balance modelling and freshwater flux for 2007, and in a 1995–2007 perspective, *Hydrol. Processes*, *23*(17), 2470–2484, doi:10.1002/hyp.7354.

Nakamura, N., and A. H. Oort (1988), Atmospheric heat budgets of the polar-regions, *J. Geophys. Res.*, *93*(D8), 9510–9524, doi:10.1029/JD093iD08p09510.

Nghiem, S. V., I. G. Rigor, D. K. Perovich, P. Clemente-Colón, J. W. Weatherly, and G. Neumann (2007), Rapid reduction of Arctic perennial sea ice, *Geophys. Res. Lett.*, *34*, L19504, doi:10.1029/2007GL031138.

O'Dwyer, J., Y. Kasajima, and O. Nøst (2001), North Atlantic Water in the Barents Sea Opening, 1997 to 1999, *Polar Res.*, *20*, 209–216, doi:10.1111/j.1751-8369.2001.tb00058.x.

Ono, N. (1967), Specific heat and heat of fusion of sea ice, in *Physics of Snow and Ice*, edited by H. Oura, pp. 599–610, Inst. of Low Temp. Sci., Hokkaido, Japan.

Popova, E. E., A. Yool, A. C. Coward, Y. K. Aksenov, S. G. Alderson, B. A. de Cuevas, and T. R. Anderson (2010), Control of primary production in the Arctic by nutrients and light: Insights from a high resolution ocean general circulation model, *Biogeosciences*, *7*(11), 3569–3591, doi:10.5194/bg-7-3569-2010.

Rabe, B., U. Schauer, A. Mackensen, M. Karcher, E. Hansen, and A. Beszczynska-Möller (2009), Freshwater components and transports in the Fram Strait - recent observations and changes since the late 1990s, *Ocean Sci.*, *5*(3), 219–233, doi:10.5194/os-5-219-2009.

Rabe, B., M. Karcher, U. Schauer, J. M. Toole, R. A. Krishfield, S. Pisarev, F. Kauker, R. Gerdes, and T. Kikuchi (2011), An assessment of Arctic Ocean freshwater content changes from the 1990s to the 2006–2008 period, *Deep Sea Res., Part I*, *58*, 173–185, doi:10.1016/j.dsr.2010.12.002.

Røed, L. P., and J. Albretsen (2007), The impact of freshwater discharges on the ocean circulation in the Skagerrak/northern North Sea area. Part I: Model validation, *Ocean Dyn.*, *57*, 269–285, doi:10.1007/s10236-007-0122-5.

Rudels, B., E. Fahrbach, J. Meincke, G. Budéus, and P. Eriksson (2002), The East Greenland Current and its contribution to the Denmark Strait overflow, *ICES J. Mar. Sci.*, *59*, 1133–1154, doi:10.1006/jmsc.2002.1284.

Rudels, B., G. Björk, J. Nilsson, P. Winsor, I. Lake, and C. Nohr (2005), The interaction between waters from the Arctic Ocean and the Nordic Seas north of Fram Strait and along the East Greenland Current: Results from the ArcticOcean-02 Oden expedition, *J. Mar. Syst.*, *55*(1–2), 1–30, doi:10.1016/j.jmarsys.2004.06.008.

Rudels, B., M. Marnela, and P. Eriksson (2008), Constraints on estimating mass, heat and freshwater transports in the Arctic Ocean: An exercise, in *Arctic-Subarctic Ocean Fluxes: Defining the Role of the Northern Seas in Climate*, edited by R. R. Dickson, J. Meincke, and P. Rhines, pp. 315–341, Springer, Dordrecht, Netherlands.

Sætre, R. (1999), Features of the central Norwegian shelf circulation, *Cont. Shelf Res.*, *19*(14), 1809–1831, doi:10.1016/S0278-4343(99)00041-2.

Schauer, U., and A. Beszczynska-Möller (2009), Problems with estimation and interpretation of oceanic heat transport—Conceptual remarks for the case of Fram Strait in the Arctic Ocean, *Ocean Sci.*, *5*(4), 487–494, doi:10.5194/os-5-487-2009.

Schauer, U., H. Loeng, B. Rudels, V. K. Ozhigin, and W. Dieck (2002a), Atlantic Water flow through the Barents and Kara Seas, *Deep Sea Res., Part I*, *49*(12), 2281–2298, doi:10.1016/S0967-0637(02)00125-5.

Schauer, U., B. Rudels, E. P. Jones, L. G. Anderson, R. D. Muech, G. Bjork, J. H. Swift, V. Ivanov, and A. M. Larsson (2002b), Confluence and redistribution of Atlantic water in the Nansen, Amundsen and Marakov basins, *Ann. Geophys.*, *20*, 257–273, doi:10.5194/angeo-20-257-2002.

Schauer, U., E. Fahrbach, S. Osterhus, and G. Rohardt (2004), Arctic warming through the Fram Strait: Oceanic heat transport from 3 years of measurements, *J. Geophys. Res.*, *109*, C06026, doi:10.1029/2003JC001823.

Schauer, U., A. Beszczynska-Möller, W. Walczowski, E. Fahrbach, J. Piechura, and E. Hansen (2008), Variation of measured heat flow through the Fram Strait between 1997 and 2006, in *Arctic-Subarctic Ocean Fluxes: Defining the Role of the Northern Seas in Climate*, edited by R. R. Dickson, J. Meincke, and P. Rhines, pp. 65–85, Springer, Dordrecht, Netherlands.

Serreze, M. C., A. P. Barrett, A. G. Slater, R. A. Woodgate, K. Aagaard, R. B. Lammers, M. Steele, R. Moritz, M. Meredith, and C. M. Lee (2006), The large-scale freshwater cycle of the Arctic, *J. Geophys. Res.*, *111*, C11010, doi:10.1029/2005JC003424.

Serreze, M. C., A. P. Barrett, A. G. Slater, M. Steele, J. Zhang, and K. E. Trenberth (2007), The large-scale energy budget of the Arctic, *J. Geophys. Res.*, *112*, D11122, doi:10.1029/2006JD008230.

Serreze, M. C., A. P. Barrett, J. C. Stroeve, D. N. Kindig, and M. M. Holland (2009), The emergence of surface-based Arctic amplification, *Cryosphere*, *3*(1), 11–19, doi:10.5194/tc-3-11-2009.

Shiklomanov, A. I., and R. B. Lammers (2009), Record Russian river discharge in 2007 and the limits of analysis, *Environ. Res. Lett.*, *4*(4), 045015, doi:10.1088/1748-9326/4/4/045015.

Skagseth, Ø., T. Furevik, R. B. Ingvaldsen, H. Loeng, K. A. Mork, K. A. Orvik, and V. Ozhigin (2008), Volume and heat transports to the Arctic Ocean via the Norwegian and Barents seas, in *Arctic-Subarctic Ocean Fluxes: Defining the Role of the Northern Seas in Climate*, edited by R. R. Dickson, J. Meincke, and P. Rhines, pp. 45–64, Springer, Dordrecht, Netherlands.

Skagseth, Ø., K. F. Drinkwater, and E. Terrile (2011), Wind- and buoyancy-induced transport of the Norwegian Coastal Current in the Barents Sea, *J. Geophys. Res.*, *116*, C08007, doi:10.1029/2011JC006996.

Sloyan, B. M., and S. R. Rintoul (2001), The Southern Ocean limb of the global deep overturning circulation, *J. Phys. Oceanogr.*, *31*(1), 143–173, doi:10.1175/1520-0485(2001)031<0143:TSOLOT>2.0.CO;2.

Smedsrud, L. H., R. Ingvaldsen, J. E. O. Nilsen, and Ø. Skagseth (2010), Heat in the Barents Sea: Transport, storage, and surface fluxes, *Ocean Sci.*, *6*(1), 219–234, doi:10.5194/os-6-219-2010.

Steele, M., R. Morley, and W. Ermold (2001), PHC: A global ocean hydrography with a high-quality Arctic Ocean, *J. Clim.*, *14*(9), 2079–2087, doi:10.1175/1520-0442(2001)014<2079:PAGOHW>2.0.CO;2.

Steele, M., J. Morison, W. Ermold, I. Rigor, M. Ortmeyer, and K. Shimada (2004), Circulation of summer Pacific halocline water in the Arctic Ocean, *J. Geophys. Res.*, *109*, C02027, doi:10.1029/2003JC002009.

Tang, C. C. L., C. K. Ross, T. Yao, B. Petrie, B. M. DeTracey, and E. Dunlap (2004), The circulation, water masses and sea-ice of Baffin Bay, *Prog. Oceanogr.*, *63*(4), 183–228, doi:10.1016/j.pocean.2004.09.005.

Timco, G. W., and R. M. W. Frederking (1996), A review of sea ice density, *Cold Reg. Sci. Technol.*, *24*, 1–6, doi:10.1016/0165-232X(95)00007-X.

Topp, R., and M. Johnson (1997), Winter intensification and water mass evolution from yearlong current meters in the Northeast Water Polynya, *J. Mar. Syst.*, *10*(1–4), 157–173, doi:10.1016/S0924-7963(96)00083-8.

van den Broeke, M., J. Bamber, J. Ettema, E. Rignot, E. Schrama, W. J. van de Berg, E. van Meijgaard, I. Velicogna, and B. Wouters (2009), Partitioning recent Greenland mass loss, *Science*, *326*, 984–986, doi:10.1126/science.1178176.

Velicogna, I. (2009), Increasing rates of ice mass loss from the Greenland and Antarctic ice sheets revealed by GRACE, *Geophys. Res. Lett.*, *36*, L19503, doi:10.1029/2009GL040222.

Vinje, T., N. Nordlund, and A. Kvambekk (1998), Monitoring ice thickness in Fram Strait, *J. Geophys. Res.*, *103*(C5), 10,437–10,449, doi:10.1029/97JC03360.

Woodgate, R. A., and K. Aagaard (2005), Revising the Bering Strait freshwater flux into the Arctic Ocean, *Geophys. Res. Lett.*, *32*, L02602, doi:10.1029/2004GL021747.

Woodgate, R. A., K. Aagaard, and T. J. Weingartner (2005), Monthly temperature, salinity, and transport variability of the Bering Strait through flow, *Geophys. Res. Lett.*, *32*, L04601, doi:10.1029/2004GL021880.

Woodgate, R. A., K. Aagaard, and T. J. Weingartner (2006), Interannual changes in the Bering Strait fluxes of volume, heat and freshwater between 1991 and 2004, *Geophys. Res. Lett.*, *33*, L15609, doi:10.1029/2006GL026931.

Woodgate, R. A., T. J. Weingartner, T. E. Whitledge, R. Lindsay, and K. Crane (2008), The Pacific gateway to the Arctic—Quantifying and understanding Bering Strait oceanic fluxes. Russian American long-term census of the Arctic, report, NOAA, Silver Spring, Md. [Available at http://www.arctic.noaa.gov/aro/russian-american/2008/THE_PACIFIC_GATEWAY_TO_THE_ARCTIC.pdf.]

Woodgate, R. A., T. Weingartner, and R. Lindsay (2010), The 2007 Bering Strait oceanic heat flux and anomalous Arctic sea-ice retreat, *Geophys. Res. Lett.*, *37*, L01602, doi:10.1029/2009GL041621.

Wunsch, C. (1996), *The Ocean Circulation Inverse Problem*, 442 pp., Cambridge Univ. Press, Cambridge, U. K., doi:10.1017/CBO9780511629570.

Zhang, J., and D. Rothrock (2003), Modeling global sea ice with a thickness and enthalpy distribution model in generalized curvilinear coordinates, *Mon. Weather Rev.*, *131*(5), 845–861, doi:10.1175/1520-0493(2003)131<0845:MGSIWA>2.0.CO;2.

Y. Aksenov, S. Bacon, and T. Tsubouchi, National Oceanography Centre, Southampton, European Way, Southampton SO14 3ZH, UK. (tt2r07@noc.ac.uk)

A. Beszczynska-Möller and E. Fahrbach, Alfred Wegener Institute for Polar and Marine Research, Bussestr. 24, Bremerhaven D-27570, Germany.

E. Hansen, Norwegian Polar Institute, Framsenteret, Hjalmar Johansens Gate 14, Tromsø N-9296, Norway.

R. B. Ingvaldsen, Institute of Marine Research, Box 1870 Nordnes, Bergen N-5817, Norway.

S. W. Laxon, Centre for Polar Observation and Modelling, University College London, Pearson Building, Gower Street, London WC1E 6BT, UK.

C. M. Lee, Polar Science Center, Applied Physics Laboratory, University of Washington, 1013 NE 40th St., Box 355640, Seattle, WA 98105-6698, USA.

A. C. Naveira Garabato, National Oceanography Centre, Southampton, University of Southampton, European Way, Southampton SO14 3ZH, UK.